Uranium mining fuels evolution in deep groundwater microbiomes

Wei Xiu[1,2], Till L.V. Bornemann[2], Tianjing Zhang[1], André R. Soares[2], Luping Xie[1], Julian M. Künkel[2], Guoxi Lian[3], Haicheng Weng[4], Chongsheng Lu[1,6], Bing Yang[4], Ruixuan Gai[1], Zhipeng Gao[1], Di Zhang[1], Yuan Yuan[4], Zhiming Du[4,7,8], Qingyin Xia[4], Linxing Chen[9], Jonathan R Lloyd[5], Hailiang Dong[1], Xuebin Su[10], Huaming Guo[1]*, and Alexander J. Probst[2]*

[1] *State Key Laboratory of Geomicrobiology and Environmental Changes (GMEC), China University of Geosciences, Beijing 100083, People's Republic of China*

[2] *Environmental Metagenomics, Research Center One Health Ruhr, University Alliance Ruhr, Faculty of Chemistry, University of Duisburg-Essen, Germany*

[3] *Nuclear and Radiation Safety Center, Ministry of Ecology and Environment, Beijing, 100082, China*

[4] *Beijing Research Institute of Chemical Engineering and Metallurgy CNNC, No.145 Jiukeshu, Tongzhou District, Beijing 101149, China*

[5] *Williamson Research Laboratories for Molecular Environmental Science, Department of Earth and Environmental Sciences, The University of Manchester, Manchester M13 9PL, United Kingdom*

[6] *The Institute of Hydrogeology and Environmental Geology, Chinese Academy of Geosciences, Shijiazhuang 050061, China*

[7] *China University of Petroleum, Beijing 102249, China*

[8] *National Key Laboratory of Uranium Resources Exploration-Mining and Nuclear Remote Sensing, Nanchang 330013, China*

[9] *State Key Laboratory of Advanced Environmental Technology, the Department of Environmental Science and Engineering, University of Science and Technology of China, Hefei, Anhui 230026, China*

[10] *China National Uranium Co., Ltd, Sanlihe, Xicheng District, Beijing, 100045, PR China*

* to whom correspondence should be addressed: Prof. Alexander J. Probst (alexander.probst@uni-due.de); Prof. Huaming Guo (hmguo@cugb.edu.cn)

Abstract

Deep-biosphere microbes have been underpinning global biogeochemical cycles throughout Earth history, yet their evolutionary responses to long-term anthropogenic disturbance remain poorly understood. Neutral-pH in-situ leaching (ISL), the dominant uranium-mining strategy, imposes persistent radiochemical and redox stress offering rare natural experiments across decades for observing subsurface microbial evolution. Here, by exploiting metagenomics and metatranscriptomics in examining microbial responses through various mining stages, we show that neutral U ISL causes substantial changes in microbial communities spanning 2,294 strains accompanied by diversification and selection of active microbial species. These changes occurred during elevated dissolved uranium and radiological activity which correlated with a substantial transcriptional change in energy metabolism, and with an overexpression of specific genes for oxidative-stress defence and DNA-repair pathways. Increased nucleotide diversity in 101 out of 392 species clusters and nonsynonymous/synonymous polymorphism ratios greater than one in 139 species clusters were predominantly observed in metatranscriptomes with elevated radiation, highlighting positive selection of transcriptionally active populations. These findings demonstrate that neutral U ISL drives functional and genetic diversification of subsurface microbiomes, revealing a dynamic and evolutionarily responsive deep biosphere.

Introduction

Microbial consortia in the deep subsurface, adapted to nutrient-scarce, anoxic environments[1–4], mediate critical biogeochemical processes and help maintain groundwater quality[5–8]. However, anthropogenic stresses arising from mining, groundwater extraction, and energy production are perturbing these fragile environments at increasing rates[9]. Recent studies have shown that environmental stresses, including heavy metal contamination and altered pH, affect groundwater microbial communities[10,11]. Mining operations are particularly disruptive, as they rapidly subject pristine subsurface ecosystems to heavy metals, radioactive contaminants, altered redox conditions, and electrochemical gradients[9]. As mining encroaches on fragile groundwater ecosystems, resolving the evolutionary responses of subsurface microbiomes is essential for predicting the long-term consequences of resource extraction. Notably, a recent study in the abyssal seafloor showed that deep-sea mining can cause biological disruptions persisting for decades[12], underscoring the need to assess long-term impacts of subsurface resource extraction on microbiomes. Although distinct from the deep subsurface examined here, this finding underscores how resource extraction can impose long-lasting impacts on microbial communities in Earth's hidden biomes.

In-situ leaching (ISL), a widely used uranium (U) mining technique, is based on injecting oxidizing agents into aquifers to mobilize U by oxidizing insoluble U(IV) to soluble U(VI). In addition to fundamentally altering groundwater chemistry[13], this activity imposes profound chemical and radiological stresses on microbial communities that have evolved over a long time under stable and reducing conditions. Whereas the environmental consequences of ISL are well documented mostly via 16S rRNA gene analysis[11,14–16], the evolutionary responses of microbial communities to these stressors remain poorly understood. Indeed, while mining-driven alterations to groundwater chemistry are expected to disrupt the microbial community structure, functional potential, and genetic diversity[17–20], the question remains as to whether anthropogenic stress can drive microbial evolution in deep aquifers.

To this end, we implement metagenomic and metatranscriptomic strategies to examine microbial community dynamics and evolutionary adaptations at the first large-scale, neutral-pH ISL operation in China, which uses CO_2 and O_2 as leaching agents and targets a sandstone-hosted uranium deposit. It involved sampling aquifers spanning pre-mining, active mining, and post-mining phases. Leveraging this rare

sampling opportunity to study microbial adaptation as a response to mining and associated geochemical changes, we show that increases in Eh and the accompanying rise in oxidative stress, including U release and associated radioactivity, are linked to restructuring of microbial communities, enhanced oxidative-stress and DNA-repair responses, and alterations in genetic diversity. Elevated pN/pS ratios (the ratio of the rates of non-synonymous (pN) and synonymous (pS) polymorphism) and shifts in nucleotide diversity implicate mining-induced environmental gradients in significantly altering microbial evolutionary processes. Our findings yield new insights into how deep subsurface microbiomes structurally and evolutionally adapt to anthropogenic stress, bearing implications for global biogeochemical cycles, ecosystem resilience, and bioremediation strategies. The findings of this investigation underscore the consequences of uranium ISL on the evolution of subsurface life, offering a novel framework for appraising microbial resilience and adaptation in mining-impacted deep subsurface ecosystems.

RESULTS

Geochemical and radiological alterations during and following Uranium ISL

Neutral pH uranium *in-situ* leaching (neutral-pH ISL) commences while the aquifer is in its natural state (pre-mining phase), proceeds through the injection of leaching solutions (mining phase), and concludes with natural restoration efforts upon cessation of mining activities (post-mining phase; *Figs. 1a-b*). We characterized the geochemical and radiological shifts across all phases of neutral-pH ISL by collecting 80 groundwater samples from four distinct mining sites in Qianjiadian sandstone-hosted uranium deposit in China, tapping aquifers at 220-460m depth below surface (*Figs. 1b-c*). These sites underwent neutral-pH ISL for varying durations, creating a unique time-resolved dataset with considerable variation in their redox conditions, from neutral-reducing pre-mining (BG, baseline groundwater) to weakly acid-oxidizing during mining (MT, mining groundwater), and back to neutral-reducing post-mining (PMI, PMIS, and PMS, representing initial, intermediate, and stable post-mining phases, respectively; *Fig. 1c*).

Geochemical and radiological profiles shifted markedly across the pre-mining, mining and post-mining stages of neutral-pH ISL. During the pre-mining phase, groundwater was neutral-reducing (Fig. *1d*), with low total dissolved U (TU, 0.44 ± 0.31 mg/L; Fig. 1h). The aquifer was enriched in electron donors, including dissolved

organic carbon (DOC, 5.26 ± 3.51 mg/L), Fe(II) (0.85 ± 1.11 mg/L), ammonium (0.73 ± 0.70 mg/L), and sulfide (0.92 ± 1.18 mg/L) (Fig. 1f,S1), conditions that favour the reductive immobilization of U and are consistent with ongoing U mineralization under reducing conditions. In the mining phase, the injection of CO_2 and O_2 coincided with a clear oxidative shift, marked by significant increases in Eh (Fig. *1d*) and a rapid rise in TU (Fig. *1h*), which peaked after approximately four years (12.44 ± 5.04 mg/L in S3a_MT04; S3a_MT04, $n = 6$ vs. S3a_BG, $n = 5$; Kruskal–Wallis with Dunn's post hoc test, $p = 0.003$) before declining gradually from MT5 to MT20 (Fig. *1h*). Radiological activity increased in parallel, with elevated gross β and gross (α+β) signals (Figs. *1i–k*). Bicarbonate concentrations also rose significantly (Fig. *1g*), and both sulfate and nitrate increased in mid-mining stages (Fig. *S1* and Table *S1*). Following neutral-pH ISL decommissioning, groundwater shifted toward reducing conditions, with significant decreases in Eh across MT15 compared with all post-mining groups (S3b_PMI, S3b_PMIS, and S3b_PMS; Kruskal-Wallis with Dunn's post hoc test, $p < 0.001$; Fig. 1d) and corresponding declines in TU (S3b_MT15 vs. S3b_PMS; ANOVA with Tukey's test, $p = 0.036$; Fig. *1h*). This transition from oxic to anoxic conditions was further reflected by decreases in sulfate, and sulfate/Cl ratio, whereas Fe(II) concentrations increased, although these changes were not statistically significant (Fig. *S1* and Table *S1*). TU concentrations did not return to pre-mining levels (*Fig. 1h*), indicating incomplete restoration of the aquifers' original geochemical conditions.

Correlation analysis identified significant Spearman associations among major geochemical and radiological parameters (Fig. *S2*). TU showed strong positive correlations with bicarbonate ($\rho = 0.43$, n = 80, $p < 0.0001$), sulfate ($\rho = 0.65$, n = 80, $p < 0.0001$), and nitrate ($\rho = 0.69$, n = 80, $p < 0.0001$). In addition, TU exhibited positive correlations with gross α (ρ = 0.24, n = 80, $p < 0.0001$), gross β ($\rho = 0.24$, n = 80, $p < 0.0001$), and gross (α+β) ($\rho = 0.24$, n = 80, $p < 0.0001$). These relationships summarize the major covariation patterns among dissolved uranium, radiological activity, and oxidized anions across all samples.

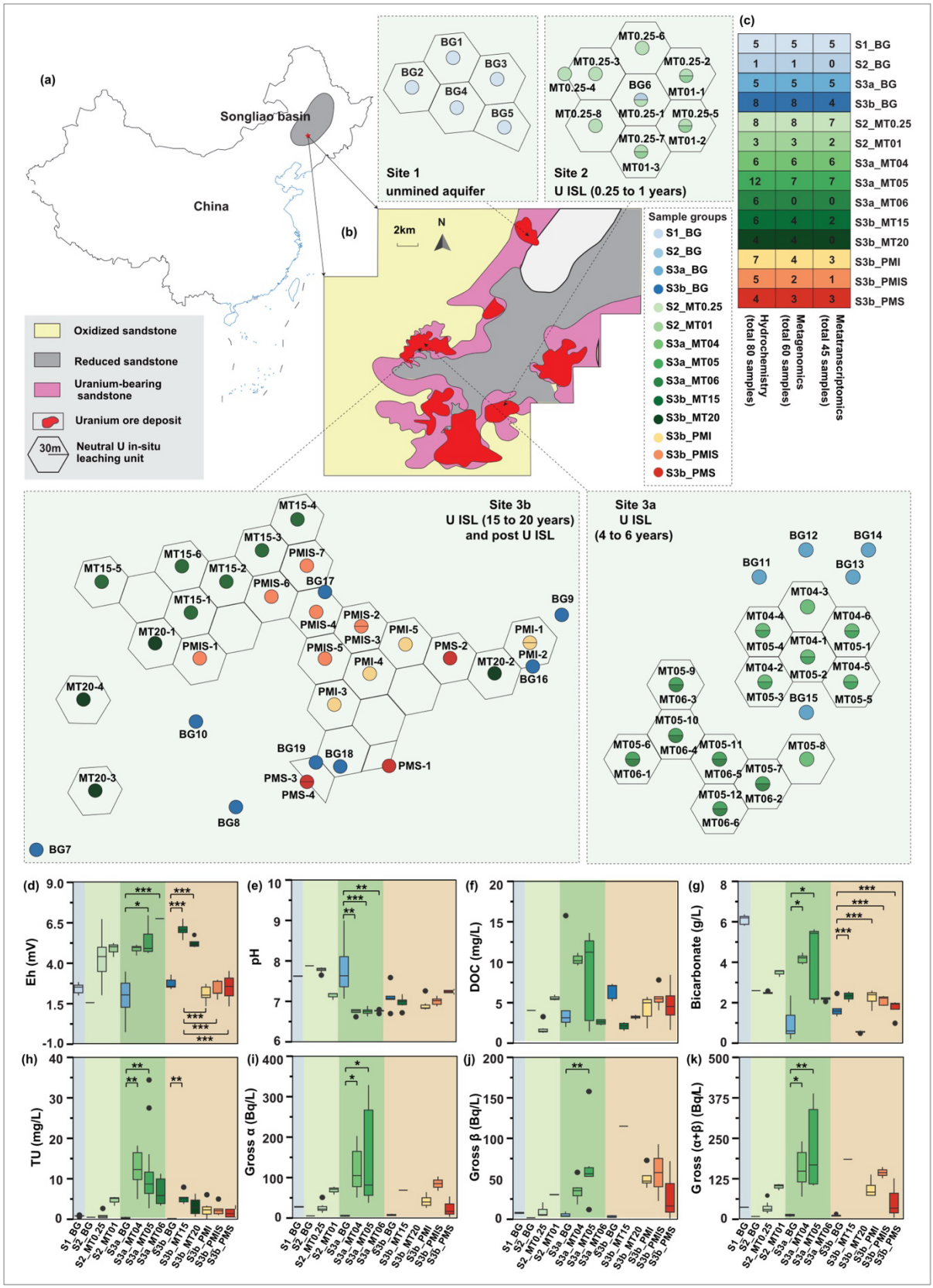

Figure 1 | Sampling locations and study overview and geochemical profiles of groundwater across neutral-pH ISL phases. *(a) Geographic location of the Songliao Basin and broader regional context, modified from a previously published source[24]. (b)*

Schematic layout of study sites along a neutral-pH ISL chronosequence: Site 1 (unmined aquifer, S1_BG); Site 2 (unmined aquifer, S2_BG; recent ISL at 0.25-1 years: S2_MT0.25 and S2_MT01); Site 3a (unmined aquifer, S3a_BG; intermediate ISL, 4-6 years: S3a_MT04, S3a_MT05, and S3a_MT06); and Site 3b (unmined aquifer, S3b_BG; long-term ISL, 15-20 years: S3b_MT15 and S3b_MT20; and decommissioned neutral-pH ISL under iron-reducing, S3b_PMI, mixed iron- and sulfate-reducing, S3b_PMIS, and sulfate-reducing, S3b_PMS conditions). Wells shown with two names indicate that the same well was sampled at different time points. The background map shows oxidized sandstone (yellow), reduced sandstone (grey), uranium-bearing sandstone (pink), uranium ore deposits (red), and neutral-pH ISL units (arrow pointers). (c) Numbers of groundwater samples collected for hydrochemical, metagenomic, and metatranscriptomic analyses across stages of neutral-pH ISL. Boxplots show geochemical parameters through the stage of neutral-pH ISL, including pre-mining (BG), mining (MT), and post-mining (PM). Panels (d – k) represent Eh, pH, DOC, bicarbonate, TU, gross α, gross β, and gross (α+β), respectively. Statistical significance was determined by ANOVA with Tukey's or Kruskal-Wallis with Dunn's test (BH-corrected), depending on data normality. Colors indicate study sites: light blue (Site 1), light green (Site 2), medium green (Site 3a), and beige (Site 3b). Blue boxplots within the studied sites (S2_BG, S3a_BG, and S3b_BG) represent the geochemical parameters from unmined aquifer samples.

Metagenome-assembled genomes reveal microbiome changes and enhanced co-occurence resulting from *in-situ* mining activity

Sixty groundwater samples representative of the pre-mining, mining, and post-mining phases across more than 20 years of neutral-pH ISL were metagenomically sequenced (Figs. *1b,c*). Exceeding 75% of sequencing coverage, based on Nonpareil estimates, indicated a sufficient depth to accurately reflect the aquifer microbiome diversity (Fig. *S3*). To assess both bacterial and archaeal diversity, we focused first on analyzing the ribosomal protein S3 gene (*rpS3*)[21] yielding 12,972 sequences that clustered (at 99% similarity) into 6,487 representative sequences spanning 215 distinct phyla (21 archaeal and 194 bacterial; Fig. *S4*). Microbial diversity also showed strong positive associations with uranium concentration and radioactivity, with prolonged neutral-pH ISL (S3a_MT04 and S3a_MT05) exhibiting significantly higher Shannon and Invsimpson indices (ANOVA with Tukey's post hoc test, $p < 0.05$; Fig.

191 *S5*). Groundwater microbial community composition and alpha diversity, based on
192 *rpS3* gene profiles, were strongly influenced by geochemical gradients, particularly
193 radiochemical activity, with higher diversity and distinct community structures
194 observed under elevated stress conditions (*Figs. S5,S6)*, as supported by *Bioenv*
195 analysis (R^2 = 0.051).
196 We reconstructed 4,075 medium-quality metagenome-assembled genomes
197 (MAGs; completeness ≥ 50%, contamination < 10%)[22], from which 2,294 strain-cluster
198 representative MAGs (strain-cluster rMAGs, 99% ANI) were obtained, with
199 *Acidobacteriota* representing the most abundant phylum (Figs. *3a-b*). These included
200 1,239 high-quality and 1,155 medium-quality strain-cluster rMAGs bearing a median
201 completeness of 94.2%, contamination level of 1.3%, and N50 of 47,633 (Figs. *3c-d*
202 and *Table* S2). Consistent with known genome-size differences between domains,
203 archaeal strain-cluster rMAGs had substantially smaller genome sizes than bacterial
204 ones (two-tailed Welch's t-test, $p < 0.0001$; Fig. *3e*), the largest genome representing
205 an organism from the family *Polyangiaceae* (12.28 Mbp). These strain-cluster rMAGs
206 spanned 63 of the 215 *rpS3*-detected phyla (29.3% of total phylum richness) yet
207 represented 75.1% of the *rpS3*-based phylum-level abundance, thereby providing a
208 robust representation of the predominant microbial communities (*Fig. S7*). The
209 remaining 70.7% of phyla, comprising the 24.9% of *rpS3*-based abundance, were not
210 captured in the strain-cluster rMAGs, potentially reflecting their lower abundance
211 and/or genomes that did not meet medium-quality criteria.
212

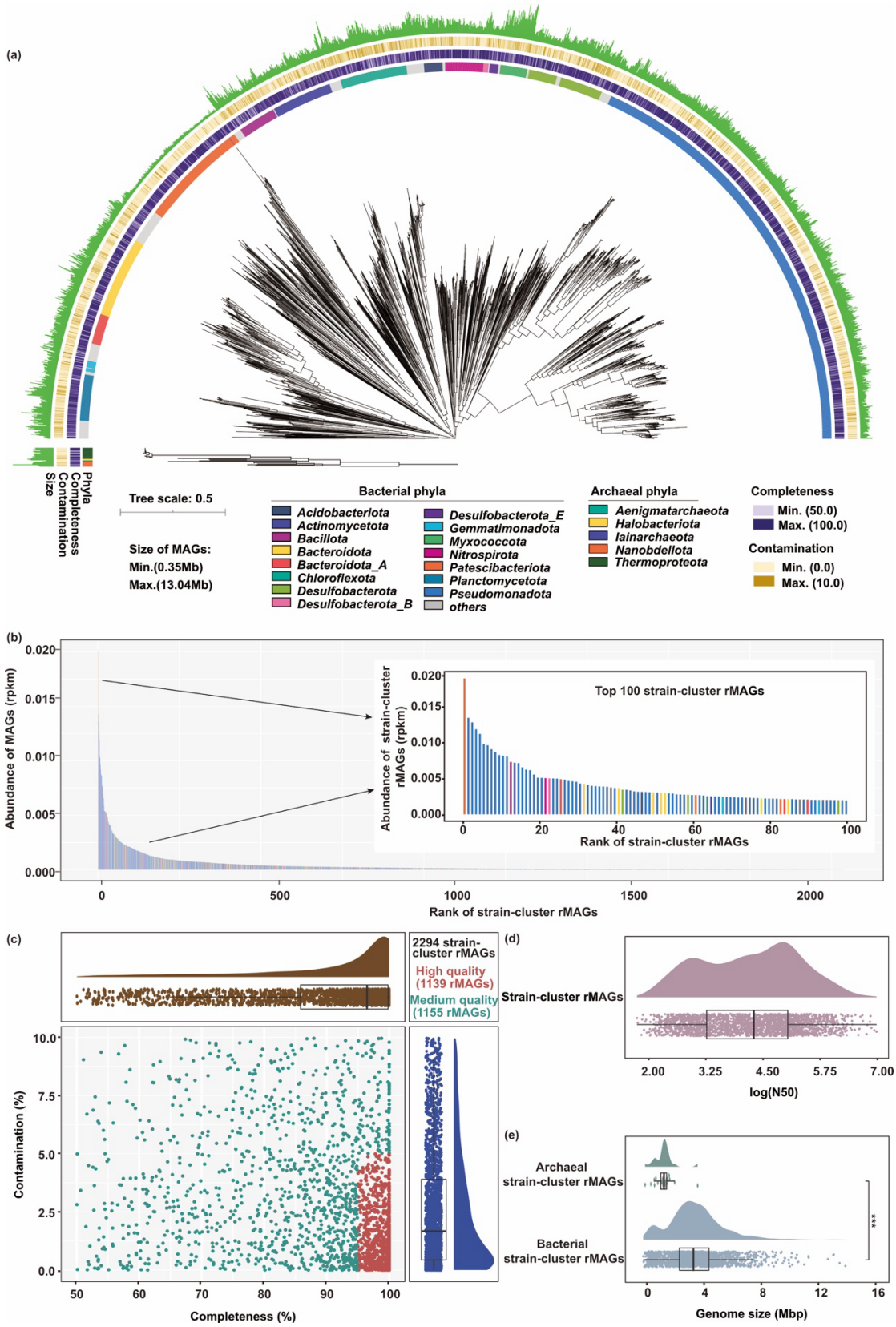

Figure 3 | Phylogenetic diversity, abundance patterns, and genomic characteristics of dereplicated strain-cluster representative MAGs. *(a) Maximum-likelihood phylogenetic tree of 2,294 dereplicated bacterial and archaeal strain-cluster*

rMAGs constructed. Outer rings indicate strain-cluster rMAG taxonomic affiliation at the phylum level (innermost ring), estimated completeness, contamination, and genome size (outermost green bars). (b) Rank abundance of strain-cluster rMAGs across phyla, with the top 100 depicted in more detail. The displayed abundances represent the average strain-cluster rMAG abundances across all samples. (c) Strain-cluster rMAGs completeness and contamination by quality tier. (d) Distribution of log(N50) values of strain-cluster rMAGs. (e) Genome size comparison between archaeal and bacterial strain-cluster rMAGs. Note that two rMAGs showed long-branch or model-sensitive placements; these were retained for completeness but do not affect the overall phylogenetic structure.

Microbial community composition, based on the relative abundance of strain-cluster rMAGs, shifted markedly along the neutral-pH ISL chronosequence (Fig. *S8*), as evidenced by sample-to-sample Spearman correlation analyses (Fig. *4a*) and non-metric multidimensional scaling (NMDS; Fig. *4b*). Communities from pre-mining, mining, and post-mining stages formed distinct clusters, with analysis of similarities (ANOSIM) indicating significant separation between stages (Fig. *4c*), reflecting divergent community trajectories during and after ISL. Network analysis of relative abundances of strain-cluster rMAGs revealed positive correlations, accounting for 90.39% of all edges, defined as significant correlations between taxa, dominating microbial interactions (Fig. *4d*). Four distinct modules (from Mod1 to Mod4) were identified. Mod1 remained stable across all ISL stages, consistent with a core community. Mod2 and Mod4 increased only during the early ISL stages, reflecting short-term adaptive responses. In contrast, Mod3 showed a sustained increase during the mining and post-mining phases, indicative of recovery processes and stress-driven selection for taxa better adapted to prolonged radiochemical and redox stress (Figs. 4f-i). Within-module degree (Zi) and particitation coefficient (Pi) analysis identified two module hubs (two strain-cluster rMAGs classified within the *Algoriphagus* and *Paracoccus*) that structured interactions within Mod4, and three connector hubs (three strain-cluster rMAGs classified within *Pseudotabrizicola*, *Burkholderiaceae* MESE01, and *Nocardioides*) that linked multiple modules. In addition, 341 peripheral connectors ($Zi \leq 2.5$ and $Pi > 0.62$) were dominated by Mod3 (175 strain-cluster rMAGs) and Mod2 (129 strain-cluster rMAGs) (Fig. *4e*), indicating that most cross-module interactions are mediated by diffuse peripheral taxa rather than by central hub nodes. These

results highlight the significant shifts in microbial community structure, diversity, and ecological interactions imposed by neutral-pH ISL. The observed tendency towards positive interactions emphasizes the dynamic and evolving nature of subsurface microbiomes in response to acute environmental stress.

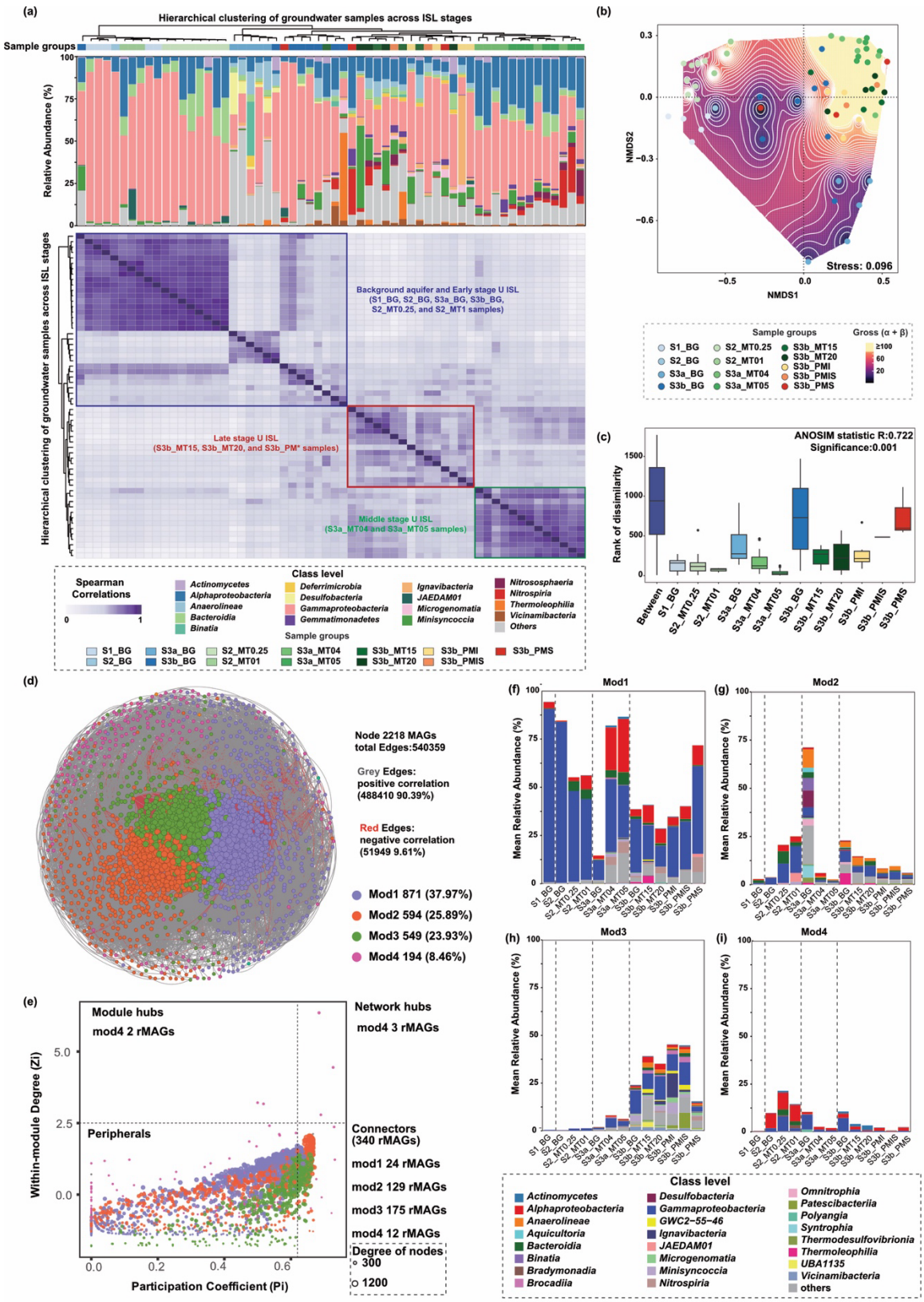

Figure 4 | Microbial community structure and modularity across neutral-pH ISL phases. *(a) Heatmap of sample-to-sample Spearman's rank correlations of strain-cluster rMAG abundances across early (blue), mid (green), and late (red) neutral-pH U ISL stages. The accompanying bar chart shows the top 12 classes across samples,*

arranged in the same sample order as in the heatmap. (b) Non-metric multidimensional scaling (NMDS) plot of community structure based on strain-cluster rMAGs (stress = 0.096). Background colors represent gross (α+β) radiation levels across all groups (interpolated across the ordination space using inverse distance weighting (IDW). Gross (α+β) radiation levels below 100 Bq/L are shown as a continuous gradient, while gross (α+β) radiation levels ≥100 Bq/L are displayed as a solid yellow. White contour lines and labels indicate gross (α+β) isopleths (Bq/L). (c) Analysis of Similarity (ANOSIM) showing significant differences between groups. (d) Network of strain-cluster rMAGs co-occurrence, with positive (grey) and negative (red) Spearman correlations grouped into four modules. Node size is proportional to the degree (number of connections). (e) Within-module degree (Zi) and participation coefficient (Pi) analysis of the network to identify the peripherals, connectors, module hub and network hubs. The size and color of the nodes are proportional to its corresponding degree and module in the network, respectively. (f-i) Distribution of the abundance of module-specific taxa across neutral-pH ISL phases for Mod1 to Mod4.

Neutral-pH ISL impacts gene expression linked to DNA repair, oxidative stress, and biogeochemical cycling

To resolve microbial functional responses to prolonged neutral-pH ISL, we analyzed metatranscriptomes from 45 genomically resolved communities spanning the pre-mining, mining, and post-mining phases. Integration of transcript profiles with 2,294 functionally annotated strain-cluster rMAGs identified 350,588 of 8,422,368 representative genes showing at least two-fold upregulation relative to the mean expression of 30S ribosomal protein genes, which served as an internal benchmark for transcriptional activity. The transcriptional landscape of entire communities based on strain-cluster rMAGs showed clear patterns of transcriptionally up-regulated populations that are specific for the sample groups across the mining sites (Fig. *S9*). Among 350,588 upregulated genes of the rMAGs, 5,677 genes were associated with carbon, hydrogen, oxygen, nitrogen, sulfur, and iron biogeochemical transformations, 4,624 with DNA repair pathways, and 2,760 with oxidative stress responses (Figs *S10-S17*), highlighting broad activation of redox and genome-stability pathways under ISL-induced chemical and radiological stress.

Regarding microbial activity of biogeochemical transformations, the expression patterns across the 5,677 related genes were strongly structured by geochemical

conditions, as revealed by *Bioenv* analysis, which identified pH, Eh, sulfide, sulfate and bicarbonate as the principal geochemical variables shaping the transcriptional structure of overexpressed C-H-O-N-S-Fe metabolic genes across the metatranscriptomes (R^2 = 0.39), with PCoA accounting for 36.9% of the variation among overexpressed genes (Figs. *5a* and *S9*). This pattern is consistent with CO_2 and O_2 injection and with oxidation of ammonium and pyrite as dominant ISL reactions fueling microbial redox metabolism. TU concentrations were moderately and positively correlated with the expression of 20 energy-conserving genes distributed across 220 strain-cluster rMAGs, including *ccoN* (cytochrome *c* oxidase, aerobic respiration; ρ = 0.44, p = 0.029; encoded in 77 strain-cluster rMAGs), *pmoC* (particulate methane monooxygenase, methane oxidation; 21 strain-cluster rMAGs), *nxrAB* (nitrite oxidoreductase, nitrite oxidation; $\rho > 0.53$, $p < 0.006$; *nxrA* in 21 and *nxrB* in 27 strain-cluster rMAGs), and *soxAYZ* (sulfur oxidation complex, sulfur oxidation; $\rho > 0.41$, $p < 0.038$; *soxA* in 43, *soxY* in 69, and *soxZ* in 74 strain-cluster rMAGs) (Figs. *5d-f* and *S16-S17*). These relationships highlight a broad activation of energy-yielding redox pathways along radiochemical gradients, underscoring the metabolic coupling of carbon, nitrogen, and sulfur cycling with oxidative stress.

In addition to metabolic adjustments, microbial populations showed dynamic transcriptional regulation of DNA-repair and oxidative-stress pathways in response to radiochemical gradients. The *Bioenv* analysis identified pH, Eh, sulfide, ammonium, and bicarbonate as the main variables structuring DNA-repair gene expression (4,624 genes, R^2 = 0.40; PCoA explained 31.7% of variance), whereas pH, Eh, sulfide, sulfate, and bicarbonate were key for the 2,760 oxidative-stress-response genes (R^2 = 0.37; PCoA explained 45.2% of variance; Figs. *5b,c*). At the individual gene level, expression of foxE (c-type cytochrome involved in Fe(II) oxidation) correlated positively with gross β and gross (α+β) (Spearman, $p < 0.05$; 8 strain-cluster rMAGs; Figs. *5b-e*), consistent with Fe redox processes being stimulated by oxygen ingress and the resulting shifts in uranium speciation and radiological activity. Consistent with these environmental associations, expressions of DNA-damage-repair genes, including *mutM* (DNA glycosylase; base-excision repair of oxidized bases; ρ = 0.43-0.49, p = 0.021-0.047; 68 rMAGs), *dam* (DNA adenine methylase; mismatch-repair guidance; ρ = 0.45-0.51, p = 0.016-0.038; 37 rMAGs), and *alkC* (alkylation-repair protein; ρ = 0.45-0.46, p = 0.034-0.038; 4 rMAGs), were positively correlated with TU and gross α, β, and (α+β) (Spearman correlations, $p < 0.05$; *Figs. 5b-e*). Notably, *mutM*

expression correlated moderately with both TU (ρ = 0.41, n = 26, p = 0.0435) and gross (α + β) (ρ = 0.51, n = 2,632, p = 0.0084; Fig. *5e*). These coordinated transcriptional patterns indicate widespread modulation of genome-stability and redox-defense mechanisms, coupling Fe redox metabolism, oxidative stress responses, and DNA repair under sustained radiochemical and geochemical stress in the aquifer.

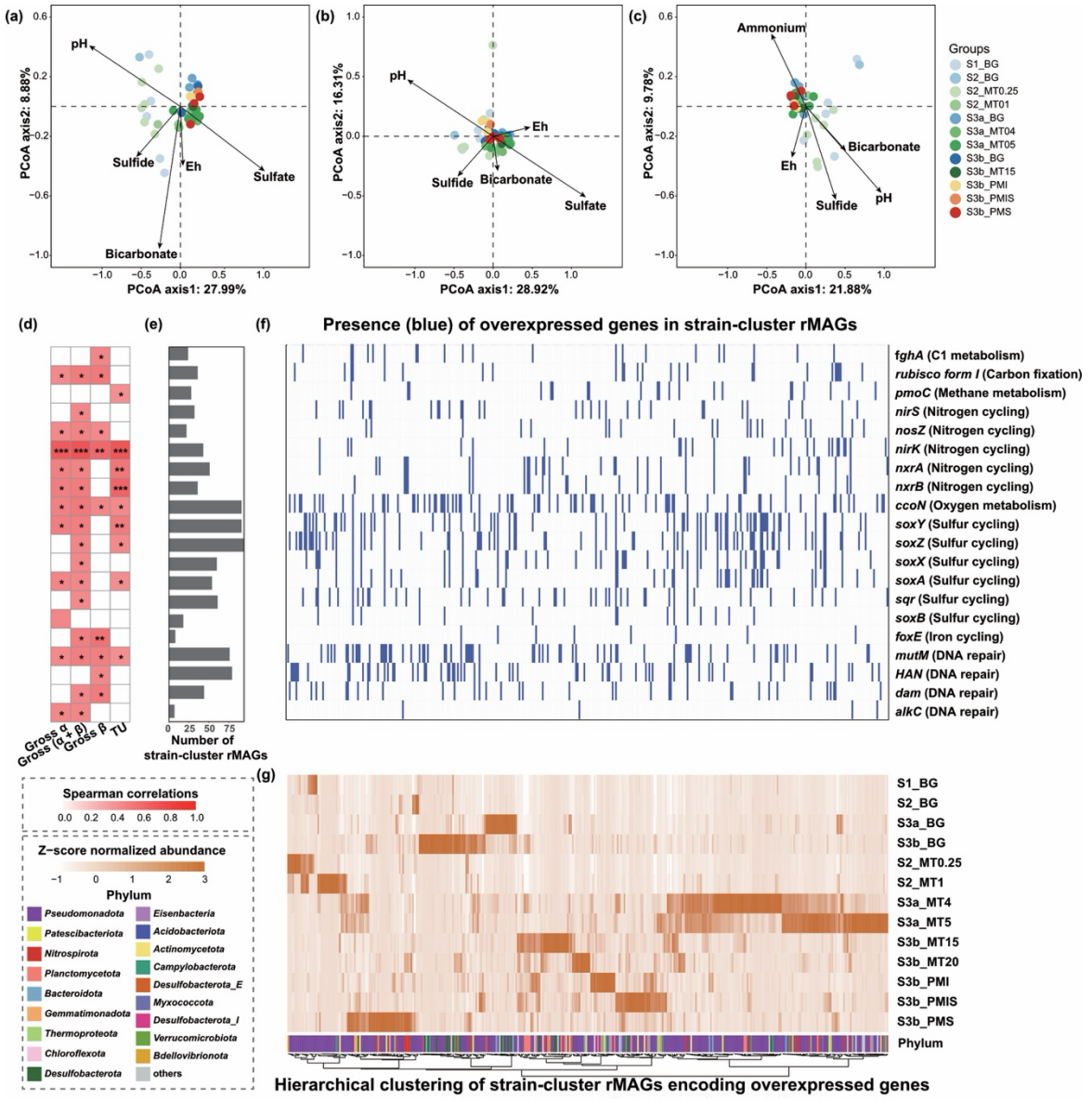

Figure 5 | Correlation and environmental drivers of overexpressed genes in metatranscriptomic datasets. *(a–c) Principal coordinate analyses (PCoA) based on expression of (a) genes involved in carbon, hydrogen, oxygen, nitrogen, sulfur, and iron metabolism, (b) DNA-repair genes, and (c) oxidative-stress-response genes. Arrows indicate environmental variables significantly correlated with gene-expression patterns, as identified by Bioenv analysis. Points are colored and shaped by sample*

342 *groups. (d) Spearman correlations of overexpressed genes positively associated with*
343 *total dissolved uranium (TU), gross α, gross β, and gross (α+β). (e) Number of strain-*
344 *cluster rMAGs encoding the corresponding overexpressed genes that are positively*
345 *correlated with total dissolved uranium (TU), gross α, gross β, and gross (α+β). (f)*
346 *Presence-absence heatmap of overexpressed genes across strain-cluster rMAGs. (g)*
347 *Z-score–normalized relative abundances of strain-cluster rMAGs encoding genes*
348 *positively correlated with TU and radiological activity (gross α, gross β, and gross (α+β))*
349 *across neutral-pH ISL stages. rMAGs are clustered by Z-score profiles, with phylum-*
350 *level taxonomy indicated below.*
351
352 **Uranium ISL-induced stress drives genetic diversification in subsurface**
353 **aquifers**
354 Within-species selection pressure and genetic diversity were quantified across
355 2402 members of 392 dereplicated species-cluster rMAGs (95% ANI). Each rMAG
356 was represented by more than three members with >5× genome coverage in 60
357 metagenomic and 45 metatranscriptomic datasets, spanning neutral-pH ISL phases,
358 enabled direct comparisons of genomic and transcriptional diversity across mining
359 stages.
360 NMDS analysis of pN/pS ratios revealed a clear progression from background
361 to mining and post-mining samples in both metagenomes (Fig. *6h*) and
362 metatranscriptomes (Fig. *6j*), closely aligned with increasing TU concentrations.
363 Consistent with this ordination, site-level analyses showed that the median
364 metagenomic pN/pS ratios increased in early mining, late mining, and post-mining
365 sites and metatranscriptomic pN/pS ratios exhibited similar but stronger increases (p
366 < 0.05, *Figs. 6a-c*). *Bioenv* analysis identified gross α, gross (α+β), Eh, TFe, TU,
367 ammonium, Fe(II), nitrite, and nitrate as the main correlates of metagenomic pN/pS
368 (R^2 = 0.28), and gross β, gross (α+β), TDS, TU, and ammonium for the
369 metatranscriptomes (R^2 = 0.23), indicating that mutation–selection imbalance reflects
370 the combined influence of the oxidizing geochemical regime and co-varying metal and
371 radionuclide stress. Instances of positive selection (pN/pS > 1) were more frequent in
372 the metatranscriptomes (139 MAG clusters) than in the metagenomes (112 MAG
373 clusters) or in both datasets combined (49 MAG clusters; Fig. *S19*), highlighting
374 intensified adaptive pressures on actively expressed genomes.

To explore whether these shifts in selection were supported by changes in standing genetic variation, we next examined genome-wide nucleotide diversity across species-cluster rMAGs. NMDS ordinations revealed a consistent progression from background to mining and post-mining samples in both metagenomes and metatranscriptomes, closely tracking TU gradients (*Figs. 6g-j*). Metagenomic nucleotide diversity remained relatively stable during the mid-mining phase but declined in early-, late-, and post-mining stages despite sustained TU concentrations. (Figs. *6d-f*). By contrast, metatranscriptomic nucleotide diversity rose sharply during the mid-mining phase at site S3a ($p < 0.001$; Fig. *6e*), coinciding with peak uranium and radioactivity. Bioenv analysis identified radioactivity (gross α, gross β, and gross (α+β)) and geochemical parameters (Eh, TFe, TU, ammonium, Fe(II), and nitrate) as key correlates of metagenomic genome-wide nucleotide diversity ($R^2 = 0.25$), with comparable associations in metatranscriptomes (gross β, gross (α+β), TDS, TU, and ammonium; $R^2 = 0.21$). Together, these patterns indicate that prolonged uranium-mining stress maintains elevated genetic variation in transcriptionally active populations, consistent with bet-hedging-like strategies that enhance adaptive flexibility in fluctuating radiochemical environments.

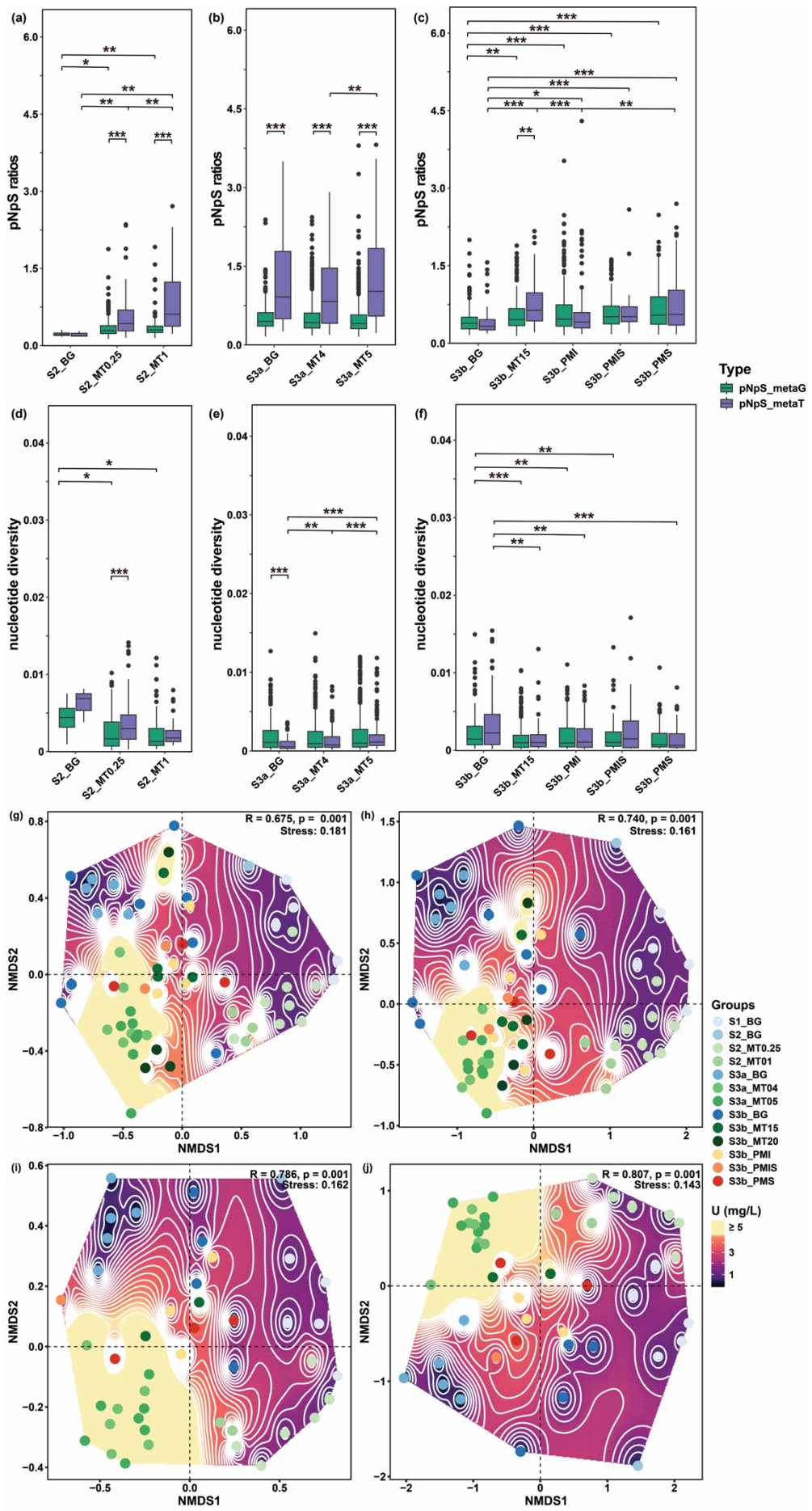
(a)
(b)
(c)
pNpS ratios
S2_BG
S2_MT0.25
S2_MT1
S3a_BG
S3a_MT4
S3a_MT5
S3b_BG
S3b_MT15
S3b_PMI
S3b_PMIS
S3b_PMS
Type
pNpS_metaG
pNpS_metaT
(d)
(e)
(f)
nucleotide diversity
(g)
R = 0.675, p = 0.001
Stress: 0.181
(h)
R = 0.740, p = 0.001
Stress: 0.161
(i)
R = 0.786, p = 0.001
Stress: 0.162
(j)
R = 0.807, p = 0.001
Stress: 0.143
NMDS1
NMDS2
Groups
S1_BG
S2_BG
S2_MT0.25
S2_MT01
S3a_BG
S3a_MT04
S3a_MT05
S3b_BG
S3b_MT15
S3b_MT20
S3b_PMI
S3b_PMIS
S3b_PMS
U (mg/L)
≥ 5
3
1

392

Figure 6 | Genome-wide pN/pS ratio and nucleotide diversity across mining stages in metagenomes and metatranscriptomes. *(a-c) pN/pS ratio from metagenomic (metaG) and metatranscriptomic (metaT) datasets spanning pre-mining, mining, and post-mining phases; (d-f) Nucleotide diversity from metaG and metaT datasets across neutral-pH ISL stages; (g-j) Non-metric multidimensional scaling (NMDS) plots based on Bray–Curtis dissimilarity showing the relationships between TU and pN/pS ratios or nucleotide diversity derived from metaG (g, h) and metaT (i, j) datasets.Statistical significance was assessed using the Kruskal–Wallis test followed by Dunn's post-hoc test with Benjamini–Hochberg (BH) correction for multiple comparisons (* $p < 0.05$, ** $p < 0.01$, and *** $p < 0.001$).*

Sixty-five out of 392 species clusters exhibited recurrent increases in nucleotide diversity from background to mining-impacted conditions, including 20 detected in both metagenomic and metatranscriptomic datasets (Figs. *7a,b*). Four representative taxa, *Kuenenia* (rMAG-1), *Gallionella* (rMAG-2 and rMAG-4), and *Parvibaculum* (rMAG-3), persisted across all mining phases and exhibited elevated genome-wide diversity in both metagenomic and metatranscriptomic datasets. Gene-level diversification was dispersed across loci rather than confined to specific genomic regions, with hundreds of variable genes per genome (rMAG-1: 269/1,126; rMAG-3: 95/148; rMAG-4: 213/280; rMAG-2: 295/350) and substantial overlap between genomic and transcriptomic variation, indicating that many variable loci were transcriptionally active, particularly within core functional networks linked to uranium-induced stress responses, including information processing, regulation, and stress adaptation (*Fig. 7c*). *Kuenenia* rMAG-1 exhibited genomic diversification in hydroxylamine dehydrogenase (*hao*) and hydrazine dehydrogenase (*hdh*) genes mediating ammonium oxidation, together with *lexA* (SOS-response regulator involved in DNA damage repair), *old-family endonuclease* (genome maintenance), *lon* (ATP-dependent protease for protein quality control), and *tolC* (outer-membrane efflux channel for metal detoxification). The two *Gallionella* rMAGs displayed contrasting transcriptional responses. The rMAG-2 showed variability in redox-related genes, including cytochrome-c oxidase cbb3-type subunit II (*fixO*), involved in microaerobic respiration and electron transport, and *thioredoxin-dependent peroxiredoxin*, linked to reactive oxygen species metabolism under oxidative stress. By contrast, rMAG-4 exhibited transcript-level variability in outer-membrane porins (*ompC*/*ompF*/*phoE*) associated with metal-regulated

permeability, the conjugal transfer protein *traF* involved in horizontal gene transfer, and glycosyltransferases contributing to cell-envelope remodeling. *Parvibaculum* rMAG-3 encoded a GIY–YIG endonuclease, associated with the cleavage of damaged or mismatched DNA, and a Zn-dependent protease involved in protein quality control under oxidative stress, including conditions where metal exposure can exacerbate ROS damage. Together, these diversification patterns suggest that persistent taxa employ distinct, lineage-specific strategies-spanning redox flexibility, oxidative defense, membrane adaptation, and proteogenomic repair, to maintain resilience under the combined chemical and radiochemical stresses imposed by U mining.

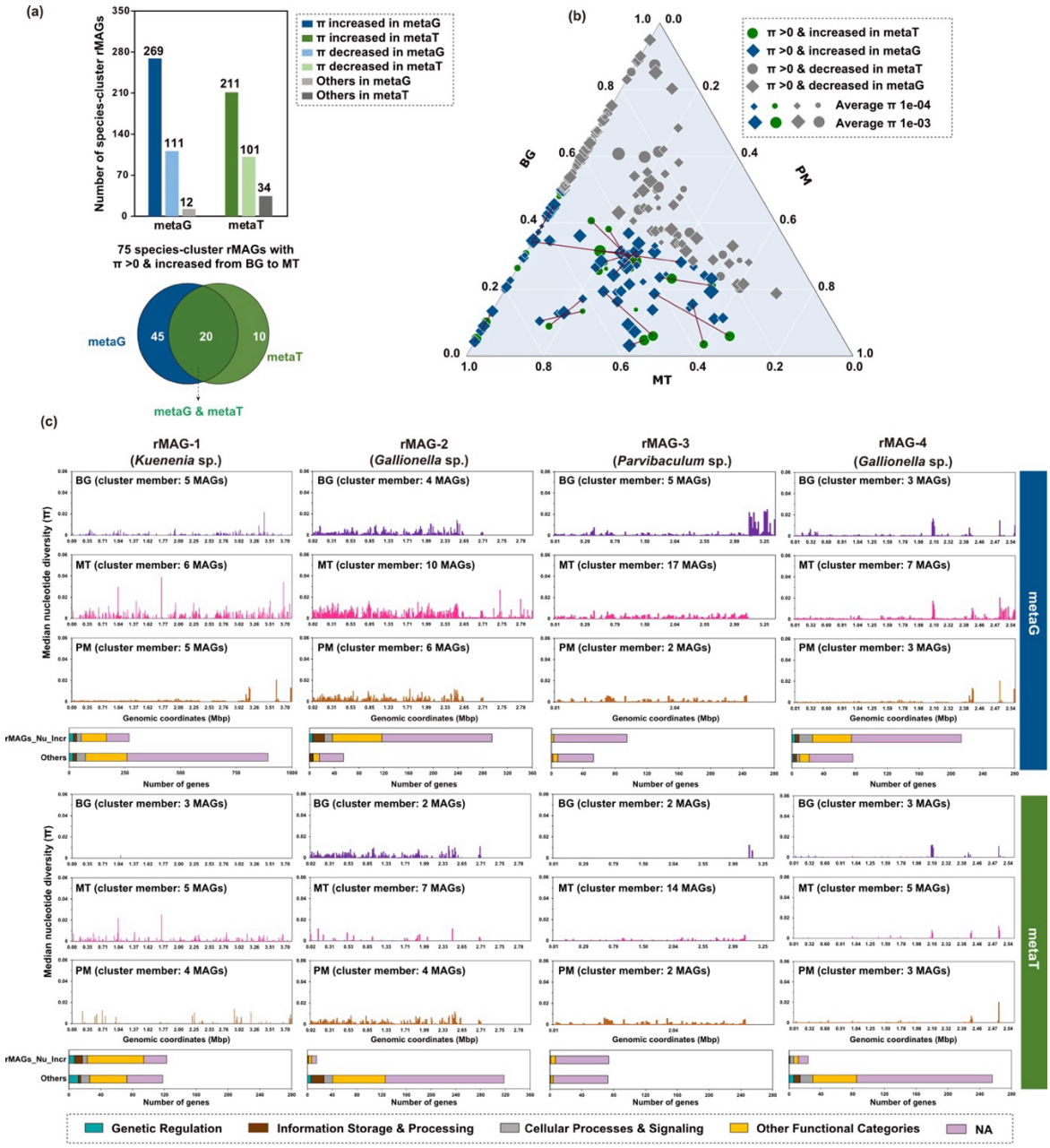

Figure 7 | Genome-wide nucleotide diversity patterns across mining stages in representative rMAGs. *(a) Bar plots show the total numbers of species-cluster rMAGs with increased or decreased nucleotide diversity (π) from background (BG) to mining (MT) conditions in metagenomic (metaG) and metatranscriptomic (metaT) datasets. Increased π indicates rMAGs with callable nucleotide diversity (≥ 5× coverage) in MT samples but either non-callable diversity (< 5× coverage) or lower π values in BG samples; decreased π follows the inverse criterion. The accompanying Venn plot displays the overlap of rMAGs with increased π (π > 0) between the metaG and metaT datasets. (b) Ternary plot showing the distribution of rMAG-level nucleotide diversity across BG, MT, and post-mining (PM) samples, with points colored by dataset and sized by diversity magnitude. (c) Gene-level nucleotide diversity profiles for four representative species-cluster rMAGs (Parvibaculum, Kuenenia, and Gallionella) across BG, MT, and PM phases. Each profile represents the median π of all cluster members for a given gene, highlighting elevated and widespread diversification during mining (MT), particularly in transcriptionally active genes. Bar plots below each panel show the functional distribution of genes with increased diversity categorized by major gene functions.*

Discussion

The global resurgence of nuclear energy has renewed interest in U ISL, a minimally invasive yet chemically intensive extraction method, poised to dominate future uranium supply chains[23,24]. During mining, strong oxidants drove the oxidation of U(IV) to U(VI) and the formation of soluble uranyl–carbonate complexes, while concurrent oxidation of pyrite and ammonium produced the elevated sulfate and nitrate characteristic of mining phases[25,26]. Following ISL cessation, DOM degradation re-established reducing conditions, accompanied by rising Fe(II) and declines in Eh, TU and sulfate, patterns consistent with Fe(III) and sulfate reduction and the partial reductive attenuation of U(VI)[27]. While such geochemical perturbations and ecological restructuring during U ISL are increasingly recognized[13,17–20,25,27–30], its evolutionary consequences for subsurface microbiomes remain underexplored. Here, we present metagenomic and metatranscriptomic evidence that neutral-pH U ISL exerts sustained selective pressure on microbial populations, driving *in situ* evolution within deep aquifers.

471 Neutral-pH ISL establishes persistent redox disequilibria through oxidant
472 injection, mobilizing U, radionuclides, and heavy metals[13,25,27–30]. By examining a
473 neutral-pH ISL area with aquifers having undergone different time periods of leaching
474 (up to 20-years), we reveal that these sustained geochemical disturbances go beyond
475 restructuring of microbial community composition and alter transcriptional activity,
476 along with an increased genetic diversity, illuminating long-term ecological and
477 evolutionary consequences for deep biosphere microbiomes. These transformations
478 are shaped by sustained selection pressures imposed by neutral-pH ISL, including
479 oxidative stress, redox-active metal toxicity, and low-dose radiation, stressors known
480 to destabilize cellular systems and promote adaptive traits linked to stress tolerance,
481 DNA repair, and redox regulation[31–33]. Comparable patterns of stress-driven
482 adaptation have been reported in acid mine drainage biofilms[34,35], heavy-metal
483 tailings[36,37], permafrost thaw soils[38], and deep-sea sediments[39,40]. Consistent with
484 these analogs, we detected increased taxonomic diversity in neutral-pH ISL-impacted
485 aquifers, signatures consistent with stress-induced diversification to increase
486 resilience at the community level[11,41–45]. Temporal succession revealed dynamic
487 microbial responses, with oxidative-stress-tolerant taxa dominating early neutral-pH
488 ISL stages and anaerobic fermenters and metal reducers emerging post-mining,
489 reflecting adaptation to evolving redox conditions.
490 Crucially, these ecological transitions were accompanied by molecular
491 signatures of adaptation. Genes associated with oxidative damage, heavy metal
492 toxicity, and radiation exposure were broadly overexpressed across all neutral-pH ISL
493 stages (*Figs. S9-S17*), indicating a constitutive stress response. Among 75 species-
494 cluster rMAGs with measurable nucleotide diversity that increased from background
495 to mining phases (Fig. 7a), many exhibited pronounced diversification along the ISL
496 gradient, suggesting that repair mechanisms were insufficient to counteract
497 accumulated genomic damage. Consequently, elevated nucleotide diversity,
498 particularly in mid-mining metatranscriptomes, supports a mutation–repair imbalance
499 in which mutational input exceeded repair capacity, consistent with a previously
500 introduced model of stress-induced mutagenesis[37,46–48]. This model posits that
501 environmentally triggered DNA damage, coupled with error-prone repair, contributes
502 to increased mutation rates. While DNA repair pathways buffer deleterious mutations,
503 they may also limit adaptive potential by constraining the fixation of beneficial
504 variants[49,50]. In our study, concurrent increases in nucleotide diversity and

505 transcriptional upregulation of DNA repair and oxidative stress-response genes
506 indicate that adaptive evolution is concentrated in metabolically active, redox-cycling
507 taxa rather than uniformly across the whole community. This resolves the modest
508 community-wide transcriptional changes yet strong gene-level positive selection
509 signals, highlighting that long-term ISL creates evolutionary hotspots where
510 radiochemical stress and altered substrate availability jointly promote adaptation in
511 key biogeochemical taxa.

512 Further support for this mechanism comes from elevated pN/pS ratios (>1), a
513 canonical signal of positive selection, observed predominantly in metatranscriptomes
514 (139 species-cluster rMAGs, including 251 and 40 cluster members were oberved in
515 mining and post-mining samples) and only partially overlapping with metagenomic
516 datasets (49 species-cluster rMAGs; Fig. S19). The rMAGs exhibiting elevated
517 nucleotide diversity encompassed phylogenetically diverse taxa and displayed
518 extensive gene-level variation in information processing and regulatory functions,
519 underscoring that selection acts primarily on transcriptionally active populations. This
520 layered response, genome-wide mutation accumulation coupled with transcription-
521 linked selection, highlights the dual role of environmental stress in both generating
522 genetic variability and filtering for functional adaptation, consistent with eco-
523 evolutionary rescue models[51–53], wherein microbial populations rebound from stress-
524 induced bottlenecks through the acquisition and retention of adaptive mutations.

525 Collectively, our study provides rare empirical evidence that stress-induced
526 mutagenesis and transcription-linked selection operate within natural deep subsurface
527 microbiomes over decadal timescales. Although such mechanisms are well
528 characterized in laboratory systems[54–60] and surface environments[46,61–64], their
529 manifestation in oligotrophic, energy-limited subsurface ecosystems[39,65–67] has
530 remained largely speculative due to assumptions of metabolic quiescence and
531 evolutionary stasis[40,68–70]. Our findings challenge this paradigm, demonstrating that
532 chronic anthropogenic stress in engineered aquifers can generate sustained
533 mutational input and facilitate directional selection. The convergence of elevated
534 nucleotide diversity, DNA repair activation, and positive selection in expressed genes
535 reveals a coordinated evolutionary response to long-term environmental disturbance.
536 These observations extend core theoretical frameworks, including stress-induced
537 mutagenesis and eco-evolutionary rescue, from controlled systems to complex,

anthropogenically modified subsurface environments, redefining the deep biosphere as a dynamic, evolutionarily responsive system.

MATERIALS AND METHODS

Study area, sampling strategy, and sample collection. The study area located in the Qianjiadian U ore deposit within the Qianjiadian (QJD) sag of the Kailu Depression in the southwestern Songliao Basin, northeast China, represents a typical sandstone-hosted U deposit[71]. The stratigraphy comprises the Qingshankou (K_2qn), Yaojia (K_2y), and Nenjiang (K_2n) formations, overlain by Neoproterozoic and Quaternary alluvial deposits. The U mineralization is primarily hosted in the K_2y Formation, which consists of red, yellow, gray, and mineralized gray sandstones, with widespread carbonate cementation (dolomite, siderite, ankerite, and calcite). Pitchblende and coffinite are the dominant uranium minerals, while Fe-Ti oxides, natural organic matter, clay minerals, and pyrite serve as additional U hosts[27,72,73]. Groundwater flow follows a southwest-to-northeast trajectory within a confined Cretaceous sandstone aquifer (approximately 298 m depth below surface, 35 m thick), with permeability averaging 0.145 m/day[25]. The aquifer is hydraulically isolated by a low-permeability mudstone-dominated aquitard both above and below, with limited connectivity to adjacent hydrogeological units.

The Qianjiadian U deposit has been a key site for advancing in-situ leaching (ISL) technology in China, serving as the first large-scale demonstration of CO_2 + O_2 leaching in a deep, low-permeability sandstone-hosted system. During the neutral-pH ISL process, the mixed reagent of dissolved O_2 (oxidant) and CO_2 (complexing agent) was injected into the ore-bearing aquifer, and subsequently, U-containing groundwater was pumped out and U was retrieved using ion exchange resins[25,74]. The effluent from the reverse osmosis system was reused as a leaching solution after being mixed with CO_2 and O_2 to maintain carbonate buffering and oxidizing conditions[75]. The orebody, located within confined sandstone aquifers at depths ranging from 220 to 460 m, presents complex hydrogeological conditions that influence solute transport, aquifer reactivity, and microbial community dynamics. The unique geological and hydrogeochemical setting of the Qianjiadian deposit, combined with its prolonged history of neutral-pH ISL operations, establishes it as a natural laboratory for investigating subsurface fluid-rock-microbe interactions, U mobilization processes,

571 and the long-term geochemical and microbial responses to neutral-pH ISL as well as
572 post-mining restoration.
573 To investigate the hydrogeochemical and microbial responses to neutral-pH ISL
574 mining, groundwater samples were collected from the Qianjiadian (QJD) sandstone-
575 hosted U deposit during two field campaigns in October-November 2021 and August-
576 October 2022 (Figure 1). A total of 80 groundwater samples were obtained from sites
577 representing different stages of neutral-pH ISL, spanning ore-bearing aquifers at
578 depths of 220-460 m. Sampling locations encompassed neutral-pH ISL sites spanning
579 multiple operational durations: 0.25 years (S2_MT0.25, 8 samples), 1 year (S2_MT01,
580 3 samples), 4 years (S3a_MT04, 6 samples), 5 years (S3a_MT05, 12 samples), 6
581 years (S3a_MT06, 6 samples), 15 years (S3b_MT15, 6 samples), and 20 years
582 (S3b_MT20, 4 samples). Post-mining phases were sampled under distinct redox
583 conditions, including iron-reducing (S3b_PMI, 7 samples), mixed iron- and sulfate-
584 reducing (S3b_PMIS, 5 samples), and sulfate-reducing (S3b_PMS, 4 samples)
585 conditions. Nineteen groundwater samples from unmined aquifer were collected
586 across the chronosequence, including non-mining areas (S1_BG, 5 samples), early-
587 stage mining sites (S2_BG, 1 sample), mid-stage mining sites (S3a_BG, 5 samples),
588 and late-stage/post-mining sites (S3b_BG, 8 samples). Background wells were
589 present at all sites and sampled concurrently with mining and post-mining wells,
590 providing site-specific baseline controls. Detailed hydrogeochemical data for
591 S3b_MT20, S3a_MT04, S3a_MT05, S3b_PMI, S3b_PMIS, S3b_PMS, and S3b_BG
592 are reported in our previous studies[25–28].
593 Prior to sample collection using a deep groundwater sampler (Geosub 2, Geotech,
594 USA), monitoring and post-mining wells were pumped for at least 20 minutes until
595 water temperature, electrical conductivity (EC), and oxidation-reduction potential
596 (ORP) stabilized. Groundwater was then pumped after well flushing and approximately
597 45 ± 0.5 L of water was filtered through 0.2-μm sterile cellulose nitrate membrane
598 filters (Sartorius, Göttingen, Germany) to capture microbial organisms from each
599 groundwater well. All filtered membranes were frozen at -80 °C for high-throughput
600 sequencing. Groundwater samples for physicochemical analysis were collected in 5 L
601 sterile PET bottles and stored at -20 °C.
602 **Chemical Analysis.** Major anions (Cl^-, NO_3^-, and SO_4^{2-}) were measured using ion
603 chromatography (Dionex ICS-600, Thermo Fisher Scientific, Massachusetts, USA),
604 while major cations (Na^+, K^+, Mg^{2+}, and Ca^{2+}) were determined using inductively

605 coupled plasma optical emission spectrometry (ICP-OES, Optima 8300, PerkinElmer,
606 Massachusetts, USA). Trace elements, including U, Fe, and other transition metals,
607 were quantified using inductively coupled plasma mass spectrometry (ICP-MS, 7900
608 ICP-MS, Agilent Technologies, California, USA). Alkalinity was measured by Gran
609 titration using a Metrohm 888 Titrando (Metrohm, Herisau, Switzerland). The total
610 organic carbon (TOC) and dissolved organic carbon (DOC) concentrations were
611 determined using a TOC analyzer (TOC-L, Shimadzu, Kyoto, Japan). The gross alpha
612 and gross beta radioactivity of groundwater samples were measured using a low-
613 background α/β meter (LB6008, Beijing Yida Measurement Technology Co., Ltd.,
614 Beijing, China) following the thick source method for radioactivity analysis, in which
615 evaporated water residues are deposited onto a planchet to form a uniform thick
616 source for α/β counting. Measurements of gross alpha and gross beta radioactivity
617 were conducted at the China Nuclear Mining Science and Technology Corporation,
618 Beijing, China, to assess radiological characteristics associated with uranium
619 mobilization.
620 **DNA extraction and sequencing.** Total metagenomic DNA was extracted from
621 biomass retained on 0.22-μm sterile cellulose nitrate membrane from 60 groundwater
622 samples, selected from a total of 80 samples retrieved from different neutral-pH ISL
623 stages in ore-bearing aquifers (see above and Figure *1b-c*). DNA extraction was
624 performed using the FastDNA® SPIN Kit for Soil (MP Biomedicals, Solon, OH, USA)
625 following the manufacturer's protocol. The concentration and purity of the DNA
626 extracts were measured using a TBS-380 fluorometer (Turner Biosystem, USA) and a
627 NanoDrop 2000 spectrophotometer (Thermo Scientific, USA), respectively. The
628 quality of the DNA extracts was checked using 1%-agarose gel electrophoresis.
629 Paired-end sequencing was performed on the Illumina HiSeq XTen platform (Illumina,
630 Inc., San Diego, CA, USA) at Majorbio Bio-Pharm Technology Co., Ltd., China. DNA
631 extracts were fragmented to an average size of approximately 400 bp using a Covaris
632 M220 ultrasonicator (Gene Company Limited, China). Paired-end libraries were
633 constructed using the NEXTFLEX Rapid DNA-Seq Kit (Bioo Scientific, Austin, TX,
634 USA), with adapters containing the full complement of sequencing primer hybridization
635 sites ligated to the blunt end of fragments.
636 **Metagenome processing and MAG recovery.** Raw reads were trimmed and quality-
637 filtered using fastp v0.19.7[83]. The microbial diversity and its coverage based on quality-
638 filtered raw metagenomic reads was estimated by Nonpareil v3.4.1[76] in "kmer" mode.

639 High-quality reads from individual samples were assembled into scaffolds using
640 metaSPAdes version 3.15.5 (--k-list 21, 33, 55, 77, 99, and 127)[77]. Open-Reading
641 Frames on scaffolds were predicted using prodigal (v2.6.3)[78] in "meta" mode. MAGs
642 were recovered from each assembly using the binning module (parameters: -metabat2
643 -maxbin2 -concoct) within metaWRAP v1.3 (metabat2 v2.12.1, MaxBin2 v.2.2.6, and
644 concoct v0.4.0)[79–82], which bins based on reads mapped only from the corresponding
645 sample. Quality of genome bins (completeness and contamination) was evaluated
646 using CheckM2 (v2.0.11)[83]. Binning results from multiple algorithms were integrated
647 using DASTool v1.1.7 with default parameters[84] to generate a non-redundant MAG
648 set for each sample. The resulting bins were further refined using itBins
649 (https://github.com/ProbstLab/itBins), and screened and cleaned for contaminant
650 sequences with the NCBI Foreign Contamination Screen (FCS-GX v0.5.5)[85]. Finally,
651 a total of 4,075 MAGs were obtained with completeness ≥50% and contamination
652 <10%. Bins were further consolidated via dereplication at strain level using dRep
653 (v.3.2.2) at 99% ANI[86] resulting in 2,294 strain-cluster representative MAGs (strain-
654 cluster rMAGs).
655 **Taxonomic classification of strain-cluster rMAGs and phylogenetic tree**
656 **generation.** Taxonomies were assigned to each strain-cluster rMAG using GTDB-Tk
657 v2.1.1 (https://github.com/Ecogenomics/GTDB-Tk, database release 226)[87].
658 Phylogenetic relationships were inferred using GTDB-Tk (v2.1.1), which identifies
659 conserved marker genes and constructs genome trees following the GTDB reference
660 framework. The resulting GTDB-based phylogenetic tree was used to resolve the
661 taxonomic placement of strain-cluster rMAGs. The phylogenetic tree was visualized
662 using the Interactive Tree of Life (iTOL)[88].
663 **Coverage estimation and metabolic potential prediction.** Clean reads from each
664 sample were mapped to strain-cluster rMAGs using strobealign (v0.13.0)[89] in CoverM
665 (v0.7.0; default parameters)[90]. The metabolic potential of strain-cluster rMAGs was
666 determined using METABOLIC v4.0[91]. We constructed two databases, one containing
667 96 genes associated with DNA repair mechanisms and one containing 32 genes
668 implicated in microbial responses to oxidative stress, with all genes being sourced
669 from NCBI (https://www.ncbi.nlm.nih.gov/). Genes of strain-cluster rMAGs were
670 annotated against these databases using DIAMOND BLAST[92] with an E-value
671 threshold of $1e^{-5}$ and the parameter -k 1 to retain only the top scoring hit. To ensure
672 the specificity of these annotations, a reverse BLAST was subsequently conducted by

673 aligning database hits back against the original amino acid sequences of the
674 corresponding strain-cluster rMAGs using the same E-value threshold. Only reciprocal
675 hits that aligned to the same ORFs as the original query were retained, ensuring one-
676 to-one correspondence. Cases with multiple high-scoring matches were excluded to
677 avoid ambiguous annotations. Final hits were filtered based on a similarity threshold
678 of >50%, ensuring high-confidence functional assignments. These curated datasets
679 facilitated a refined analysis of microbial resilience and adaptation strategies in diverse
680 environmental contexts.
681 **Community profiling based on the *rpS3* marker gene.** ORFs representing the *rpS3*
682 marker gene were identified using hmmsearch[93] against custom Hidden Markov
683 Models (HMMs) for Archaea and Bacteria (E-value $1e^{-28}$;
684 https://github.com/AJProbst/rpS3_trckr). Sequences were pooled and clustered at 99%
685 similarity using vsearch[94], representing species-level clusters[95]. Representative
686 sequences were selected following a tiered approach: (1) centroids that could be
687 extended by 1000 bp in both directions, (2) non-centroids that were similarly
688 extendable, and (3) the longest available sequence when neither of the first two criteria
689 were met. To improve abundance estimates, *rpS3* gene sequences of representative
690 *rpS3* genes were extended by up to 1,000 bp in both directions on their scaffold of
691 origin if possible. This was done as mapping on just the approximately 1,000 bp long
692 *rpS3* gene results in poor mapping on the gene edges and this has progressively more
693 impact when the total length of the sequence is short. The resulting *rpS3* gene
694 sequences, ideally extended in both directions by 1,000 bp, are henceforth called
695 *rpS3*-extended. The workflow for clustering, extracting, and calculating coverage is
696 available at https://github.com/ProbstLab/publication-
697 associated_scripts/tree/main/FigueroaGonzalez_Bornemann_etal. The *rpS3* genes in
698 *rpS3*-extended sequences (in amino acid format) were taxonomically classified using
699 DIAMOND[92] (E-value ≤ $1e^{-5}$) against the GTDB r226 protein database, assigning the
700 best hit to be the taxonomy. If no hit meeting the search criteria was found,
701 "Unclassified" was assigned. Abundance was calculated by mapping reads of all
702 metagenomic samples to *rpS3*-extended sequences and calculating the average
703 coverage per sample. Additionally, the breadth, i.e., the number of nucleotide positions
704 in *rpS3*-extended having a coverage of at least 1, was determined. The coverage of
705 an *rpS3*-extended sequence in a given sample was set to zero if the breadth of the
706 sequence in that sample was less than 95%, indicating spurious mapping instead of

707 actual presence of the *rpS3*-extended-represented species. Relative coverage values
708 were transformed into percentages (%).
709 ***RNA extraction, sequencing, and metatranscriptomics.*** Total RNA was isolated
710 and purified using Soil RNA Extraction Kit (Majorbio, Shanghai, China) following the
711 manufacturer's procedure. The integrity and quantity of the extracted RNA were
712 measured with a NanoDrop 2000 spectrophotometer (Thermo Scientific, MA, USA)
713 and an Agilent 5300 Bioanalyzer (Agilent Technologies, Palo Alto, CA, USA). The RNA
714 was subjected to standard Illumina library preparation using the Illumina® Stranded
715 mRNA Prep, Ligation kit (Illumina, San Diego, CA, USA), and rRNA was depleted
716 using a RiboCop rRNA Depletion Kit for Mixed Bacterial Samples (Lexogen, USA).
717 Depleted RNA was extracted from biomass retained on 0.22 μm sterile cellulose
718 nitrate membranes from 60 groundwater samples (same to metagenomic groundwater
719 samples) and finally library preparation of RNA extraction from 45 groundwater
720 samples were successfully constructed (Figure *1c*). Sequencing was performed on an
721 Illumina Novaseq6000 sequencer (Illumina, San Diego, CA, USA) with paired-end
722 sequencing method at Majorbio Bio-Pharm Technology Co., Ltd. (Shanghai, China).
723 Quality control of the raw data generated by sequencing was carried out with fastp
724 v0.19.7[96]. SortMeRNA (v4.3.6) was used to remove non-coding RNA sequences
725 (tRNA, tmRNA, 5S, 16S, 18S, 23S, and 28S)[97]. The proportion of reads removed per
726 sample is summarized in Supplementary Table *S3* and Figure *S20*, providing an
727 overview of rRNA/tRNA content prior to filtering.
728 ***Gene expression dynamics in metatranscriptomes.*** InStrain (v1.8.1)[98] with the
729 parameter (--min_cov 0) was used on strain-cluster rMAGs recovered from the same
730 sample to get the coverage of each gene using the clean reads from each
731 metagenome and each metatranscriptome. The gene coverage in each strain-cluster
732 rMAG was received by using the cluster database generated when dereplicate
733 genomes at 99% ANI using dRep (v3.2.2)[86]. The mean coverage of 30S ribosomal
734 proteins were used to calculate the normalization factor of each gene from the strain-
735 cluster rMAGs in each metatranscriptome sample. The genes with normalization
736 expression level greater than two were defined as overexpressed genes. The average
737 expression level of each gene in each sample was calculated and subjected to
738 Principal Coordinates Analysis (PCoA) based on Bray-Curtis dissimilarity. Average
739 gene expression levels were also used to calculate Spearman correlations with TU

740 and radioactivity. In addition, a presence-absence matrix was constructed using gene
741 annotation profiles predicted from metabolic potential analyses.
742 **Species-level clustering and calculation of evolutionary metrics.** Filtered reads
743 from each metagenome and metatranscriptome were mapped to the cleaned MAGs
744 output from FCS-GX (v0.5.5) of the same sample using strobealign (v0.13.0)[89] in
745 CoverM (v0.7.0; default parameters)[90]. Open reading frames (ORFs) of each MAG
746 were predicted using Prodigal (v2.6.3; –p single)[78] and used as input for inStrain
747 (v1.8.1)[98]. Population statistics and nucleotide metrics, including nucleotide diversity
748 (SNVs/kbp) and nonsynonymous to synonymous mutation ratios (pN/pS) were
749 calculated from these mappings using the profile module of the inStrain (v1.8.1; default
750 parameters)[98] at genome and gene levels. The 4075 MAGs reconstructed from all
751 individual assemblies (n = 60) were combined and dereplicated for species-level
752 clustering using dRep (v3.2.2)[86] at 95% ANI. A total of 1752 MAGs with the highest
753 genome quality from each species cluster were designated as the representative
754 species (species-cluster rMAGs). The species-cluster rMAGs with over three
755 members in the cluster database generated when dereplicate genomes at 95% ANI
756 were selected for the final calculation of microdiversity metrics such as coverage,
757 breadth, SNPs density, nucleotide diversity, and pN/pS ratios.
758 For SNP calling, the number of quality-filtered reads mapping to the position had to be
759 at least 5× coverage and 5% SNP frequency, and the variant based on reads had to
760 be lower than the expected sequencing error rate ($1e^{-6}$). Genome-level evolutionary
761 metrics based on both metagenomic and metatranscriptomic data from mining sites
762 were compared with those from background aquifer samples at the same location
763 (Table *S4-S5*). To assess the genomic impact of radiochemical stress, four species-
764 cluster rMAGs showing increased nucleotide diversity and detected in at least two
765 groups (BG, MT, and PM) with a minimum of three samples per group were selected.
766 Gene annotations for the four species-cluster rMAGs were generated using
767 MetaCerberus v1.3.1[99]. All member genomes within the four species-cluster were
768 used to identify representative genes using mmseqs2 v17.b804f[100], from which
769 median nucleotide diversity was calculated from both metagenomic and
770 metatranscriptomic datasets across the BG, MT, and PM groups (*Table S6-S7*).
771 **Statistical analyses and data visualization.** Spearman correlation analyses were
772 performed in the R platform (http://cran.r-project.org), with p-values adjusted using the
773 Benjamini-Hochberg procedure at a minimum significance threshold of 0.05[101]. Co-

774 occurrence networks were constructed using the *igraph* package with default
775 parameters[102]. Only Spearman correlations with p-values < 0.001 and |ρ|> 0.6
776 between pairs of rMAGs were considered statistically significant, contributing to the
777 construction of a reliable network. The resulting correlation network was imported into
778 Gephi (v0.9.2) for visualization[103]. The Spearman correlations between over-
779 expressed genes from strain-cluster rMAGs and hydrogeochemical variables were
780 visualized using the *pheatmap* package in R (v4.4.2)[104]. To assess sample similarity
781 and identify factors shaping community clustering, Principal Coordinates Analysis
782 (PCoA) and Non-metric Multidimensional Scaling (NMDS) were performed based on
783 Bray–Curtis dissimilarity of microbial community composition. Relationships between
784 geochemical parameters and biological features—including community dissimilarities,
785 gene expression levels, nucleotide diversity, and pN/pS ratios—were further evaluated
786 using *Bioenv* analysis (*vegan* package, R v4.4.2)[105], which identifies the combination
787 of environmental variables best explaining the observed biological variation.
788
789 ACKNOWLEDGEMENTS
790 This study was supported by the National Natural Science Foundation of China grant
791 nos. 42130509 (to H.G.) and 42072273 (to W.X.), the Deep Earth Probe and Mineral
792 Resources Exploration-National Science and Technology Major Project grant no.
793 2024ZD1000601 (to W.X.), the Fundamental Research Funds for the Central
794 Universities grant no. 590223006 (to W.X.) and the 111 Project grant no. B20010 (to
795 H.G.); and by the European Research Council Synergy Grant “Archean Park” under
796 grant no. 101118631 (to A.J.P.) and the German Research Foundation grant no. PR
797 1603/4-1 (to A.J.P.). We thank Prof. Rizlan Bernier-Latmani (Environmental
798 Microbiology Laboratory, École Polytechnique Fédérale de Lausanne, Switzerland) for
799 valuable comments on the manuscript and for providing access to laboratory
800 resources.
801
802 CONFLICT OF INTEREST
803 The authors declare no conflict of interest.
804
805 Ethics Statement
806 All sampling and sample collection were performed with permission from the local
807 environmental authorities and in compliance with all applicable regulations governing

environmental research in China. No human subjects or animal samples were involved in this study.

CODE AVAILABILITY STATEMENT

All code used in this manuscript is publicly available and referenced in the Materials and Methods section.

REFERENCES

1. Xie, X. *et al.* Groundwater Quality and Public Health. *Annu. Rev. Environ. Resour.* **48**, 395–418 (2023).
2. Orsi, W. D., Edgcomb, V. P., Christman, G. D. & Biddle, J. F. Gene expression in the deep biosphere. *Nature* **499**, 205–208 (2013).
3. Magnabosco, C. *et al.* The biomass and biodiversity of the continental subsurface. *Nat. Geosci.* **11**, 707–717 (2018).
4. Beaver, R. C. & Neufeld, J. D. Microbial ecology of the deep terrestrial subsurface. *ISME J.* **18**, wrae091 (2024).
5. Bornemann, T. L. V. *et al.* Genetic diversity in terrestrial subsurface ecosystems impacted by geological degassing. *Nat. Commun.* **13**, 1–12 (2022).
6. Patsis, A. C., Schuler, C. J., Toner, B. M., Santelli, C. M. & Sheik, C. S. The potential for coupled organic and inorganic sulfur cycles across the terrestrial deep subsurface biosphere. *Nat. Commun.* **16**, 3827 (2025).
7. Probst, A. J. *et al.* Differential depth distribution of microbial function and putative symbionts through sediment-hosted aquifers in the deep terrestrial subsurface. *Nat. Microbiol.* **3**, 328–336 (2018).
8. He, C. *et al.* Genome-resolved metagenomics reveals site-specific diversity of episymbiotic CPR bacteria and DPANN archaea in groundwater ecosystems. *Nat. Microbiol.* **6**, 354–365 (2021).
9. Amundson, K. K., Borton, M. A. & Wilkins, M. J. Anthropogenic impacts on the terrestrial subsurface biosphere. *Nat. Rev. Microbiol.* **23**, 147–161 (2025).
10. Vigneron, A. *et al.* Succession in the petroleum reservoir microbiome through an oil field production lifecycle. *ISME J.* **11**, 2141–2154 (2017).
11. Ning, D. *et al.* Environmental stress mediates groundwater microbial community assembly. *Nat. Microbiol.* **9**, 490–501 (2024).

12. Jones, D. O. B. *et al.* Long-term impact and biological recovery in a deep-sea mining track. *Nature* https://doi.org/10.1038/s41586-025-08921-3 (2025) doi:10.1038/s41586-025-08921-3.
13. Li, G. & Yao, J. A Review of In Situ Leaching (ISL) for Uranium Mining. *Mining* **4**, 120–148 (2024).
14. Jroundi, F. *et al.* Profiling native aquifer bacteria in a uranium roll-front deposit and their role in biogeochemical cycle dynamics: Insights regarding in situ recovery mining. *Sci. Total Environ.* **721**, (2020).
15. Vrionis, H. A. *et al.* Microbiological and geochemical heterogeneity in an in situ uranium bioremediation field site. *Appl. Environ. Microbiol.* **71**, 6308–6318 (2005).
16. Chen, H. *et al.* Uranium contamination mediating soil and ore microbial community assembly at four mining sites, South China. *Front. Microbiol.* **16**, 1553072 (2025).
17. Zhu, F., Zhao, B., Min, W. & Li, J. Characteristics of groundwater microbial communities and the correlation with the environmental factors in a decommissioned acid in-situ uranium mine. *Front. Microbiol.* **13**, 1078393 (2023).
18. Coral, T. *et al.* Microbial communities associated with uranium in-situ recovery mining process are related to acid mine drainage assemblages. *Sci. Total Environ.* **628–629**, 26–35 (2018).
19. Van Nostrand, J. D. *et al.* Dynamics of Microbial Community Composition and Function during In Situ Bioremediation of a Uranium-Contaminated Aquifer. *Appl. Environ. Microbiol.* **77**, 3860–3869 (2011).
20. Li, B. *et al.* Bacterial Community Shift and Coexisting/Coexcluding Patterns Revealed by Network Analysis in a Uranium-Contaminated Site after Bioreduction Followed by Reoxidation. *Appl. Environ. Microbiol.* **84**, e02885-17 (2018).
21. Sharon, I. *et al.* Accurate, multi-kb reads resolve complex populations and detect rare microorganisms. *Genome Res.* **25**, 534–543 (2015).
22. Bowers, R. M. *et al.* Minimum information about a single amplified genome (MISAG) and a metagenome-assembled genome (MIMAG) of bacteria and archaea. *Nat. Biotechnol.* **35**, 725–731 (2017).

23. *Energy, Electricity and Nuclear Power Estimates for the Period up to 2050*. (INTERNATIONAL ATOMIC ENERGY AGENCY, Vienna, 2024).
24. Monnet, A., Gabriel, S. & Percebois, J. Long-term availability of global uranium resources. *Resour. Policy* **53**, 394–407 (2017).
25. Lu, C. *et al.* Multi-Isotope Based Identification and Quantification of Oxygen Consuming Processes in Uranium Hosting Aquifers With $CO_2 + O_2$ In Situ Leaching. *Water Resour. Res.* **59**, e2022WR033980 (2023).
26. Lian, G. *et al.* Genome-Resolved Metagenomic Insights into Aquifer Microbiome Adaptations Following Two Decades of Neutral In-Situ Leaching. *J. Geophys. Res. Biogeosciences* **130,** e2024JG008587 (2025).
27. Lu, C. *et al.* Characteristics of Dissolved Organic Matter in Uranium Hosting Aquifers and Potential Molecular Transformation During Neutral In Situ Leaching. *J. Geophys. Res. Biogeosciences* **129**, e2023JG007851 (2024).
28. Lu, C. *et al.* Natural Attenuation of Groundwater Uranium in Post-Neutral-Mining Sites Evidenced from Multiple Isotopes and Dissolved Organic Matter. *Environ. Sci. Technol.* **58**, 12674–12684 (2024).
29. Asghar, F. *et al.* Geochemical characteristics and uranium neutral leaching through a co2 + o2 system—an example from uranium ore of the elzpa ore deposit in Pakistan. *Metals* **10**, 1–19 (2020).
30. Ruiz, O., Thomson, B., Cerrato, J. M. & Rodriguez-Freire, L. Groundwater restoration following in-situ recovery (ISR) mining of uranium. *Appl. Geochem.* **109**, 104418 (2019).
31. Wani, A. K., Akhtar, N., Sher, F., Navarrete, A. A. & Américo-Pinheiro, J. H. P. Microbial adaptation to different environmental conditions: molecular perspective of evolved genetic and cellular systems. *Arch. Microbiol.* **204**, 144 (2022).
32. Newsome, L., Morris, K. & Lloyd, J. R. The biogeochemistry and bioremediation of uranium and other priority radionuclides. *Chem. Geol.* **363**, 164–184 (2014).
33. Carvalho, F. *et al.* The environmental behaviour of uranium. *Int. At. Energy Agency* https://doi.org/Retrieved%2520from:%2520https://www.iaea.org/publications/14688/the-environmental-behaviour-of-uranium (2023) doi:Retrieved%20from:%20https://www.iaea.org/publications/14688/the-environmental-behaviour-of-uranium.

908 34. Huang, L.-N., Kuang, J.-L. & Shu, W.-S. Microbial Ecology and Evolution in the
909 Acid Mine Drainage Model System. *Trends Microbiol.* **24**, 581–593 (2016).
910 35. Chen, L. *et al.* Comparative metagenomic and metatranscriptomic analyses of
911 microbial communities in acid mine drainage. *ISME J.* **9**, 1579–1592 (2015).
912 36. Hemme, C. L. *et al.* Metagenomic insights into evolution of a heavy metal-
913 contaminated groundwater microbial community. *ISME J.* **4**, 660–672 (2010).
914 37. Pal, A., Bhattacharjee, S., Saha, J., Sarkar, M. & Mandal, P. Bacterial survival
915 strategies and responses under heavy metal stress: a comprehensive overview.
916 *Crit. Rev. Microbiol.* **48**, 327–355 (2022).
917 38. Mackelprang, R. *et al.* Metagenomic analysis of a permafrost microbial
918 community reveals a rapid response to thaw. *Nature* **480**, 368–371 (2011).
919 39. Orsi, W. D. Ecology and evolution of seafloor and subseafloor microbial
920 communities. *Nat. Rev. Microbiol.* **16**, 671–683 (2018).
921 40. Becraft, E. D. *et al.* Evolutionary stasis of a deep subsurface microbial lineage.
922 *ISME J.* **15**, 2830–2842 (2021).
923 41. Da Cruz Nizer, W. S. *et al.* Oxidative stress responses in biofilms. *Biofilm* **7**,
924 100203 (2024).
925 42. Nguyen, H., Ybarra, A., Başağaoğlu, H. & Shindell, O. Biofilm viscoelasticity and
926 nutrient source location control biofilm growth rate, migration rate, and
927 morphology in shear flow. *Sci. Rep.* **11**, 1–17 (2021).
928 43. Galhardo, R. S., Hastings ,P. J. & and Rosenberg, S. M. Mutation as a Stress
929 Response and the Regulation of Evolvability. *Crit. Rev. Biochem. Mol. Biol.* **42**,
930 399–435 (2007).
931 44. Evans, M. V. *et al.* In situ transformation of ethoxylate and glycol surfactants by
932 shale-colonizing microorganisms during hydraulic fracturing. *ISME J.* **13**, 2690–
933 2700 (2019).
934 45. Zhou, J. *et al.* Stochasticity, succession, and environmental perturbations in a
935 fluidic ecosystem. *Proc. Natl. Acad. Sci.* **111**, E836–E845 (2014).
936 46. MacLean, R. C., Torres-Barceló, C. & Moxon, R. Evaluating evolutionary
937 models of stress-induced mutagenesis in bacteria. *Nat. Rev. Genet.* **14**, 221–
938 227 (2013).
939 47. Mojica, E. A. & Kültz, D. Physiological mechanisms of stress-induced evolution.
940 *J. Exp. Biol.* **225**, jeb243264 (2022).

941 48. Couce, A. *et al.* Changing fitness effects of mutations through long-term
942 bacterial evolution. *Science* **383**, eadd1417 (2024).
943 49. Denamur, E. & Matic, I. Evolution of mutation rates in bacteria. *Mol. Microbiol.*
944 **60**, 820–827 (2006).
945 50. Maharjan, R. P. *et al.* Mutation accumulation and fitness in mutator
946 subpopulations of *Escherichia coli*. *Biol. Lett.* **9**, 20120961 (2013).
947 51. Custer, G. F., Bresciani, L. & Dini-Andreote, F. Toward an integrative framework
948 for microbial community coalescence. *Trends Microbiol.* **32**, 241–251 (2024).
949 52. Shade, A. Microbiome rescue: directing resilience of environmental microbial
950 communities. *Curr. Opin. Microbiol.* **72**, 102263 (2023).
951 53. Yamamichi, M., Letten, A. D. & Schreiber, S. J. Eco-evolutionary maintenance
952 of diversity in fluctuating environments. *Ecol. Lett.* **26**, (2023).
953 54. Jinks-Robertson, S. & Bhagwat, A. S. Transcription-Associated Mutagenesis.
954 *Annu. Rev. Genet.* **48**, 341–359 (2014).
955 55. Tenaillon, O. *et al.* Tempo and mode of genome evolution in a 50,000-
956 generation experiment. *Nature* **536**, 165–170 (2016).
957 56. Wei, W. *et al.* Rapid evolution of mutation rate and spectrum in response to
958 environmental and population-genetic challenges. *Nat. Commun.* **13**, 4752
959 (2022).
960 57. Ferrare, J. T. & Good, B. H. Evolution of evolvability in rapidly adapting
961 populations. *Nat. Ecol. Evol.* **8**, 2085–2096 (2024).
962 58. Bruckbauer, S. T. & Cox, M. M. Experimental evolution of extremophile
963 resistance to ionizing radiation. *Trends Genet.* **37**, 830–845 (2021).
964 59. Daly, M. J. A new perspective on radiation resistance based on Deinococcus
965 radiodurans. *Nat. Rev. Microbiol.* **7**, 237–245 (2009).
966 60. Pavlopoulou, A. *et al.* Unraveling the mechanisms of extreme radioresistance in
967 prokaryotes: Lessons from nature. *Mutat. Res. Mutat. Res.* **767**, 92–107 (2016).
968 61. Martincorena, I., Seshasayee, A. S. N. & Luscombe, N. M. Evidence of non-
969 random mutation rates suggests an evolutionary risk management strategy.
970 *Nature* **485**, 95–98 (2012).
971 62. Ferenci, T. Irregularities in genetic variation and mutation rates with
972 environmental stresses. *Environ. Microbiol.* **21**, 3979–3988 (2019).
973 63. Foster, P. L. Stress-Induced Mutagenesis in Bacteria. *Crit. Rev. Biochem. Mol.*
974 *Biol.* **42**, 373–397 (2007).

64. Woodcroft, B. J. *et al.* Genome-centric view of carbon processing in thawing permafrost. *Nature* **560**, 49–54 (2018).
65. Mehrshad, M. *et al.* Energy efficiency and biological interactions define the core microbiome of deep oligotrophic groundwater. *Nat. Commun.* **12**, 1–12 (2021).
66. Jones, R. M., Goordial, J. M. & Orcutt, B. N. Low Energy Subsurface Environments as Extraterrestrial Analogs. *Front. Microbiol.* **9**, 1605 (2018).
67. Hoehler, T. M. & Jørgensen, B. B. Microbial life under extreme energy limitation. *Nat. Rev. Microbiol.* **11**, 83–94 (2013).
68. Jørgensen, B. B. & Marshall, I. P. G. Slow Microbial Life in the Seabed. *Annu. Rev. Mar. Sci.* **8**, 311–332 (2016).
69. Garber, A. I., Ramírez, G. A. & D'Hondt, S. Genomic stasis over millions of years in subseafloor sediment. *Environ. Microbiol.* **26**, e16674 (2024).
70. Schopf, J. W. *et al.* Sulfur-cycling fossil bacteria from the 1.8-Ga Duck Creek Formation provide promising evidence of evolution's null hypothesis. *Proc. Natl. Acad. Sci.* **112**, 2087–2092 (2015).
71. Jia, J. *et al.* Mineralogy and geochemistry of carbonate cement in sandstone and implications for mineralization of the Qianjiadian sandstone-hosted uranium deposit, southern Songliao Basin, China. *Ore Geol. Rev.* **123**, 103590 (2020).
72. Fan, Y. *et al.* The behavior of pyrite during in-situ leaching of uranium by CO2 + O2: A case study of the Qianjiadian uranium deposit in the Songliao Basin, northeastern China. *Ore Geol. Rev.* **169**, 106085 (2024).
73. Rong, H. *et al.* Effects of basic intrusions on REE mobility of sandstones and their geological significance: A case study from the Qianjiadian sandstone-hosted uranium deposit in the Songliao Basin. *Appl. Geochem.* **120**, 104665 (2020).
74. Qiu, W. *et al.* What chemical reaction dominates the CO2 and O2 in-situ uranium leaching? Insights from a three-dimensional multicomponent reactive transport model at the field scale. *Appl. Geochem.* **148**, 105522 (2023).
75. Xu, L., Wang, H., Liu, N. & Du, Z. Waste Water Treatment of CO2 + O2 in-situ Leaching Uranium. *Uranium Min. Metall.* **31**, 96–99 (2012).
76. Rodriguez-R, L. M., Gunturu, S., Tiedje, J. M., Cole, J. R. & Konstantinidis, K. T. Nonpareil 3: Fast Estimation of Metagenomic Coverage and Sequence Diversity. *mSystems* **3**, e00039-18 (2018).

1008 77. Nurk, S., Meleshko, D., Korobeynikov, A. & Pevzner, P. A. MetaSPAdes: A new
1009 versatile metagenomic assembler. *Genome Res.* **27**, 824–834 (2017).
1010 78. Hyatt, D. *et al.* Prodigal: prokaryotic gene recognition and translation initiation
1011 site identification. *BMC Bioinformatics* **11**, 119 (2010).
1012 79. Alneberg, J. *et al.* Binning metagenomic contigs by coverage and composition.
1013 *Nat. Methods* **11**, 1144–1146 (2014).
1014 80. Kang, D. D., Froula, J., Egan, R. & Wang, Z. MetaBAT, an efficient tool for
1015 accurately reconstructing single genomes from complex microbial communities.
1016 *PeerJ* **2015**, 1–15 (2015).
1017 81. Uritskiy, G. V., DiRuggiero, J. & Taylor, J. MetaWRAP—a flexible pipeline for
1018 genome-resolved metagenomic data analysis. *Microbiome* **6**, 1–13 (2018).
1019 82. Wu, Y. W., Simmons, B. A. & Singer, S. W. MaxBin 2.0: An automated binning
1020 algorithm to recover genomes from multiple metagenomic datasets.
1021 *Bioinformatics* **32**, 605–607 (2016).
1022 83. Parks, D. H., Imelfort, M., Skennerton, C. T., Hugenholtz, P. & Tyson, G. W.
1023 CheckM:assessing the quality of microbial genomes recovered from isolates,
1024 singlecells, andmetagenomes. *Genome Res.* 1043–1055 (2015)
1025 doi:10.1101/gr.186072.114.Freely.
1026 84. Sieber, C. M. K. *et al.* Recovery of genomes from metagenomes via a
1027 dereplication, aggregation and scoring strategy. *Nat. Microbiol.* **3**, 836–843
1028 (2018).
1029 85. Astashyn, A. *et al.* Rapid and sensitive detection of genome contamination at
1030 scale with FCS-GX. *Genome Biol.* **25**, 60 (2024).
1031 86. Olm, M. R., Brown, C. T., Brooks, B. & Banfield, J. F. DRep: A tool for fast and
1032 accurate genomic comparisons that enables improved genome recovery from
1033 metagenomes through de-replication. *ISME J.* **11**, 2864–2868 (2017).
1034 87. Chaumeil, P.-A., Mussig, A. J., Hugenholtz, P. & Parks, D. H. GTDB-Tk v2:
1035 memory friendly classification with the genome taxonomy database.
1036 *Bioinformatics* **38**, 5315–5316 (2022).
1037 88. Letunic, I. & Bork, P. Interactive tree of life (iTOL) v5: An online tool for
1038 phylogenetic tree display and annotation. *Nucleic Acids Res.* **49**, W293–W296
1039 (2021).
1040 89. Sahlin, K. Strobealign: flexible seed size enables ultra-fast and accurate read
1041 alignment. *Genome Biol.* **23**, 260 (2022).

1042 90. Aroney, S. T. N. *et al.* CoverM: Read alignment statistics for metagenomics.
1043 Preprint at https://doi.org/10.48550/arXiv.2501.11217 (2025).
1044 91. Zhou, Z. *et al.* METABOLIC: high-throughput profiling of microbial genomes for
1045 functional traits, metabolism, biogeochemistry, and community-scale functional
1046 networks. *Microbiome* **10**, 1–23 (2022).
1047 92. Buchfink, B., Xie, C. & Huson, D. H. Fast and sensitive protein alignment using
1048 DIAMOND. *Nat. Methods* **12**, 59–60 (2014).
1049 93. Mistry, J., Finn, R. D., Eddy, S. R., Bateman, A. & Punta, M. Challenges in
1050 homology search: HMMER3 and convergent evolution of coiled-coil regions.
1051 *Nucleic Acids Res.* **41**, e121–e121 (2013).
1052 94. Rognes, T., Flouri, T., Nichols, B., Quince, C. & Mahé, F. VSEARCH: a versatile
1053 open source tool for metagenomics. *PeerJ* **4**, e2584 (2016).
1054 95. Ruff, S. E. *et al.* A global comparison of surface and subsurface microbiomes
1055 reveals large-scale biodiversity gradients, and a marine-terrestrial divide. *Sci.*
1056 *Adv.* **10**, eadq0645 (2024).
1057 96. Chen, S., Zhou, Y., Chen, Y. & Gu, J. Fastp: An ultra-fast all-in-one FASTQ
1058 preprocessor. *Bioinformatics* **34**, i884–i890 (2018).
1059 97. Kopylova, E., Noé, L. & Touzet, H. SortMeRNA: fast and accurate filtering of
1060 ribosomal RNAs in metatranscriptomic data. *Bioinformatics* **28**, 3211–3217
1061 (2012).
1062 98. Olm, M. R. *et al.* inStrain profiles population microdiversity from metagenomic
1063 data and sensitively detects shared microbial strains. *Nat. Biotechnol.* **39**, 727–
1064 736 (2021).
1065 99. Figueroa Iii, J. L., Dhungel, E., Bellanger, M., Brouwer, C. R. & White Iii, R. A.
1066 MetaCerberus: distributed highly parallelized HMM-based processing for robust
1067 functional annotation across the tree of life. *Bioinformatics* **40**, btae119 (2024).
1068 100. Steinegger, M. & Söding, J. MMseqs2 enables sensitive protein sequence
1069 searching for the analysis of massive data sets. *Nat. Biotechnol.* **35**, 1026–1028
1070 (2017).
1071 101. Benjamini, Y. & Hochberg, Y. Controlling the False Discovery Rate: A Practical
1072 and Powerful Approach to Multiple Testing. *J. R. Stat. Soc. Ser. B Stat.*
1073 *Methodol.* **57**, 289–300 (1995).
1074 102. Csádi, G. & Nepusz, T. The igraph software package for complex network
1075 research. *InterJournal Complex Syst.* **1695**, 1–9 (2006).

103. Bastian, M., Heymann, S. & Jacomy, M. Gephi: An open source software for exploring and manipulating networks. BT - International AAAI Conference on Weblogs and Social. *Int. AAAI Conf. Weblogs Soc. Media* 361–362 (2009).
104. Kolde, R. *Pheatmap: Pretty Heatmaps*. (2025).
105. Oksanen, J. *et al.* Vegan: community ecology package. *No Title* (2001).